JOURNAL OF GEOPHYSICAL RESEARCH, VOL. ???, XXXX, DOI:10.1029/,

A physical model for seismic noise generation by turbulent flow in rivers

Florent Gimbert[1,2], Victor C. Tsai[1,2], and Michael P. Lamb[2]

Corresponding author: F. Gimbert, gimbertf@caltech.edu

[1]Seismological Laboratory, California Institute of Technology, Pasadena CA, USA, gimbertf@caltech.edu

[2]Division of Geological and Planetary Sciences, California Institute of Technology, Pasadena CA, USA

Abstract. The hydraulic forces acting at the bed of rivers and the associated sediment transport rates are major control on river erosion, but remain challenging to measure. Previous studies suggest that the seismic noise induced by rivers may be used to infer hydraulic properties and previous theoretical work showed that a bedload sediment flux can be inverted from seismic data. However, the lack of a theoretical framework relating water flow with seismic noise prevents these studies from providing quantitative information on flow processes or accurate bedload fluxes. Here, we propose a forward model of seismic noise generated by the fluctuating forces applied on river bed grains and caused by turbulent flow velocities. In agreement with previous observations, turbulent flow induced noise operates at lower frequencies than bedload induced noise. Moreover, river-to-station distance affects turbulent flow induced noise significantly enough that turbulent flow and bedload can be characterized independently from specific seismic deployments. We show that turbulent flow causes a significant part of the seismic noise recorded at the Trisuli River in Nepal, and our model provides a noise base level from which realistic estimates of bedload fluxes can be performed from the remaining noise. At Hance Rapids in the Colorado River (USA), the water flow and bedload seismic signatures are distinct in frequency, and our model captures the peak spectrum located around 6-7 Hz and previously attributed to water flow. For these configurations of an identified turbulent flow source, we suggest that river bed stress can be inverted using our model.

1. Introduction

Water flow in rivers is governed by forces that drive flow downslope due to gravity and forces due to frictional resistance at the river bed and banks. Frictional forces at the river bed are, in turn, major controls on flow velocity, flow depth, and the rate of sediment transport (e.g., *Manning* [1891]; *Bagnold* [1966]; *Einstein and Barbarossa* [1952]). In bedrock-bed rivers, these frictional forces also control the rate of bedrock erosion by plucking of fractured rock and abrasion by impacting particles traveling in bedload or suspended load (e.g., *Whipple et al.* [2000]; *Sklar and Dietrich* [2004]; *Lamb et al.* [2008a]). Fluvial bedrock erosion, in turn, drives the evolution of landscapes with broad implications for the interplay between tectonics, climate and topography (e.g., *Howard and Kerby* [1983]; *Whipple* [2004]; *Egholm et al.* [2013]). Direct and continuous measurements of near-bed hydraulic forces and sediment transport are notoriously difficult to make, especially in mountain streams, and there is a need to develop new methods to monitor rivers remotely [*Rickenmann and Recking*, 2011; *Rickenmann et al.*, 2012; *Turowski and Rickenmann*, 2011].

Rivers generate ground vibrations over a wide range of frequencies that may be due to particle collisions during sediment transport, waves at the free surface, cavitation, and frictional forces due to turbulent water flow acting against the river bed and banks, for example. Recent work has shown the potential of using seismic devices to record ground vibrations near rivers to infer river hydrodynamics and sediment transport [*Govi et al.*, 1993; *Burtin et al.*, 2008, 2011; *Hsu et al.*, 2011; *Schmandt et al.*, 2013]. These studies report a strong correlation between seismic noise amplitude recorded at 1-100

Hz frequencies and river discharge and suggest that such an observation technique could be used to monitor force fluctuations at the river bed. In particular, the sensitivity of these observations to bedload transport is strongly supported by the observed hysteresis behavior of seismic noise power versus water discharge.

In order to invert seismic records for river hydrodynamics and sediment transport, we need mechanistic theories for the processes that generate noise in rivers, and to date only the process of noise generation by bedload transport has been modeled [*Tsai et al.*, 2012]. The modelling work of *Tsai et al.* [2012] demonstrates that the observed ground motion can be explained by a bedload seismic source, characterized by a multiplicity of single grain impact events. On the basis of this framework, bedload transport flux can be inverted from seismic observations. However, *Tsai et al.* [2012] did not consider water flow as a source of noise. A model for water flow generated noise in rivers is needed to quantitatively invert for bed stress, as well as to isolate the signal of sediment transport from seismic data. The goal of this paper is to provide such a model.

The seismic signature of water flow noise has been investigated previously at two different study sites, one in the small braided alpine stream of the "Torrent de St Pierre" [*Burtin et al.*, 2011] and the other in the Colorado River in the Grand Canyon [*Schmandt et al.*, 2013]. These specific studies, performed by deploying seismometers relatively close to the river channel (meters to tens of meters away), show that the low frequency (e.g., around 10 Hz or lower) part of the ground velocity spectrum is mainly due to water-flow-induced noise. Indeed, at these low frequencies, the authors report no hysteresis with water discharge and a maximum correlation of ground velocity power with local water flow depths. However, neither of the above mentioned studies was able to mechanistically describe and predict the cause of water flow induced seismic noise.

Of the possible mechanisms that may generate ground motion from water flow, here we focus on the generation of seismic waves in the 1-100 Hz frequency range from frictional forces at the river bed due to turbulent river flow interacting with boundary roughness caused by coarse sediment. We focus on this mechanism because 1) no models yet exist for water-flow generated seismic noise and we need a starting point, 2) bed shear stress is of interest due to its role in determining river hydraulics, sediment transport and bedrock erosion, and 3) because we believe it may be the most important water-flow noise generation mechanism for the 1-100 Hz frequency range (as discussed below). Near-bed turbulence may generate noise outside of the 1-100 Hz range (e.g., due to coherent flow structures [*Nikora*, 2011; *Marquis and Roy*, 2013; *Venditti et al.*, 2013]), however, here we focus on the 1-100 Hz frequency range because 1) it overlaps with observations of putative water-flow induced noise [*Burtin et al.*, 2008, 2011; *Schmandt et al.*, 2013], 2) it overlaps with observations of putative bedload-induced noise [*Burtin et al.*, 2008, 2011; *Hsu et al.*, 2011] for which a model for water-flow induced noise is needed to isolate the bedload signal, and 3) it is the spectral range in most rivers where turbulent flow theory is particularly well developed (i.e., the inertial subrange [*Kolmogorov*, 1941]). In addition to near-bed frictional forces, sound waves generated within the water layer are expected to be converted to seismic waves at the water-ground boundary. The potential sources of sound may be cavitation [*Whipple et al.*, 2000], i.e. the implosion of air bubbles, and/or the fluctuating internal stresses in the water caused by turbulent flow, commonly called aerodynamic or hydrodynamic sound [*Lighthill*, 1952; *Curle*, 1955]. Our preliminary analysis of this hydrodynamic contribution to seismic noise suggests that the predicted seismic noise power produced is orders of magnitude lower than recorded and can be ignored relative to other sources (Gimbert et al., Using seismic observations to quantify river mechanics: example of the "Les Bossons" river (France), *In prep.*). It is important to notice, however, that this process certainly significantly affects the water-flow-induced noise recorded by high frequency acoustic sensors deployed in situ, such as microphones [*Belleudy et al.*, 2010], but these measurments are distinct from ground-motion seismometers.

Water-flow generated ground motion may also come from processes occurring at the river's free surface. *Schmandt et al.* [2013] suggested that fluid-air interactions such as breaking waves, recorded in the air by microphone measurements, may generate significant seismic noise in the frequency range of interest. Moreover, large boulders, boulder clusters, or bedrock steps may induce gravity waves and generate pressure fluctuations at bed. From observing the recurrence time of breaking waves and roughly calculating the wavelengths associated with the gravity waves expected in Hance Rapids of Grand Canyon, USA, these processes likely occur at periods of several seconds and therefore should mainly produce seismic energy at frequencies $\leq$ 1 Hz, which is outside of our spectral range of interest.

The next section of this paper presents a new model for seismic noise generation by forces induced at the river bed through the interaction of turbulent flow and boundary roughness. Section 3 explores the model results in terms of peak frequency and amplitude for water-flow generated noise for the Trisuli River, Nepal, and compares results to the bedload-transport generated noise model of *Tsai et al.* [2012]. In Section 4 we apply the model to the field measurements performed by *Schmandt et al.* [2013] at Hance Rapids on the Colorado River. We show that the amplitude and spectral properties of forces applied by the turbulent flow on river bed grains, up to now only measurable in dedicated flume experiments [*Nelson et al.*, 2001; *Schmeeckle et al.*, 2007], can be monitored in the field using seismic observations. From the knowledge of hydrological parameters at Hance Rapids, specific features of the seismic observations reported by *Schmandt et al.* [2013] can be predicted by the water-flow-induced noise model we propose. Also, the strong dependency of our model predictions on local water flow depth supports the fact that local water flow depth or bed shear stress can be inverted from seismic measurements.

2. Model

In this section, we present the derivation of a mechanical model accounting for the first-order physics that generates water-flow-induced seismic noise in rivers in the 1-100 Hz frequency band due to turbulent water-flow interacting with roughness along the river bed. In this model, we aim to calculate the total noise power spectral density (PSD) induced at a given seismic station from stresses applied by the flow moving past spherical river-bed grains of various sizes. We assume that river-bed roughness is dominated by grain-scale roughness, which is typical for gravel-bed rivers (e.g., *Parker* [1991]).

Pressure differentials associated with the turbulent flow cause normal and shear stresses at all locations along the surface of any exposed grain. The average force resulting from the contribution of all stresses applied to a given grain is commonly described as a combination of an average drag force $\bar{F}_D$ and an average lift force $\bar{F}_L$. These force components are defined with respect to an average downstream velocity $\bar{u}_2(X_1)$ operating at elevation $X_1 = D/2$ above the bed where D is grain diameter (i.e. $\bar{u}_2(X_1)$ is aligned with the grain center) and far enough upstream of the considered grain so that the velocity field is not disturbed [*Nelson et al.*, 2001; *Schmeeckle et al.*, 2007]. $\bar{F}_D$ acts parallel to $\bar{u}_2(X_1)$ over the normal surface $A_\perp$, which corresponds to the projection of the grain on the $x_1 x_3$ plane, while $\bar{F}_L$ acts perpendicular to $\bar{u}_2(X_1)$ over the parallel surface $A_\parallel$, which corresponds to the projection of the grain on the $x_1 x_2$ plane [*Schlichting*, 1979; *Schmeeckle et al.*, 2007] (see Figure 1(a)). $\bar{F}_D$ and $\bar{F}_L$ can be written as

$$\bar{F}_D = \bar{C}_D \frac{\rho_w \bar{u}_2(X_1)^2}{2} A_\perp \quad ; \quad \bar{F}_L = \bar{C}_L \frac{\rho_w \bar{u}_2(X_1)^2}{2} A_\parallel, \tag{1}$$

where ρ_w is water density and $\bar{C}_D$ and $\bar{C}_L$ are the average, standard, drag and lift coefficients [*Schlichting*, 1979]. Because we assume spherical particles, we can consider a characteristic area A defined as $A = A_\perp = A_\parallel = \pi D^2/4$. The validity of the average drag formulation of equation 1 in open channel flow configurations is supported by laboratory measurements [*Nelson et al.*, 2001; *Schmeeckle et al.*, 2007] that report a strong linear scaling between the measured average force $\bar{F}_D$ and the square of the measured average velocity $(\bar{u}_2(X_1))^2$. However, these same experiments do not report a significant scaling between the average lift force and the average downstream velocity difference across the grain [*Nelson et al.*, 2001; *Schmeeckle et al.*, 2007], suggesting that the Bernoulli effect associated with the average velocity gradient may not be the dominant mechanism that controls the average lift force.

Seismic waves are not generated by the average forces applied on river bed grains, but instead are generated by the fluctuating forces. On the basis of laboratory measurements conducted in an open channel flow, *Schmeeckle et al.* [2007] showed that a similar description used for the average drag force (see equation 1) also can be considered for the instantaneous drag force $F_D(t) = \bar{F}_D + F'_D(t)$, where $F'_D(t)$ corresponds to the fluctuating drag force. An instantaneous drag coefficient C_D can be defined such that

$$\frac{F_D(t)}{A} = C_D \frac{\rho_w (u_2(t, X_1))^2}{2}, \tag{2}$$

where $u_2(t, X_1)$ operates directly upstream of the grain (typically one particle diameter upstream). To our knowledge, an equivalent description for the fluctuating lift force has not been proposed in the past, and a relevant instantaneous velocity that correlates with the instantaneous lift force could not be identified in the previous experiments of *Schmeeckle et al.* [2007]. Moreover, in addition to drag and lift, cross-stream force fluctuations $F'_C(t)$ (acting along direction 3, see Figure 1) are also expected to generate seismic waves. In order to realize how are the three components of the fluctuating forces incorporated into our analysis, it is convenient to first formalize the role of these different force components in generating ground motion.

From the instantaneous force history $F_i(t, \mathbf{x}_0)$ applied along direction i on a given grain located at $\mathbf{x}_0$ in the channel, the ground velocity time series $\dot{u}^g_p(t, \mathbf{x})$ along direction p and at location $\mathbf{x}$ outside the channel can be described from *Aki and Richards* [2002] by

$$\dot{u}^g_p(t, \mathbf{x}) \equiv \sum_{i=1}^{3} F_i(t, \mathbf{x}_0) \otimes \frac{dG_{pi}(t, \mathbf{x}; \mathbf{x}_0)}{dt}, \tag{3}$$

where $G_{ip}(t)$ is the displacement Green's function and $\otimes$ stands for time convolution. The associated power specral density (PSD) $P^g_{w_p}(f, \mathbf{x})$ of ground velocity $\dot{u}^g_p(t, \mathbf{x})$ is defined in the frequency domain as

$$P^g_{w_p}(f, \mathbf{x}) \equiv \frac{\overline{[\dot{u}^g_p(t, \mathbf{x})]^2_f}}{df}, \tag{4}$$

where $\overline{[\dot{u}^g_p(t)]^2_f}$ is the mean-square value of the time series $\dot{u}^g_p(t)$ once bandpass filtered within a frequency band df centered around the frequency f. The explicit role of the different force components in setting $P^g_{w_p}(f, \mathbf{x})$ can be seen by substituting equation 3 into equation 4, which leads to

$$P^g_{w_p}(f,\mathbf{x}) = 4\pi^2 f^2 \cdot \sum_{i=1}^{3}\sum_{j=1}^{3} \frac{\overline{\left[F_i(t,\mathbf{x}_0)F_j(t,\mathbf{x}_0)\right]_f}}{df} G_{pi}(f,\mathbf{x};\mathbf{x}_0)G_{pj}(f,\mathbf{x};\mathbf{x}_0), \quad (5)$$

where $G_{pi}(f) \equiv \mathcal{F}\big[G_{pi}(t)\big]$ is the Fourier transform of $G_{ip}(t)$. From equation 5, it can be seen that all three force components (i.e. i=1,2 and 3) potentially contribute to each component p of ground motion. In addition, the ground motion power in direction p is also affected by the mean-square of the cross products of the force components. Since the turbulent flow field is likely to be correlated up to the grain scale (see section 2.1), one would expect that the force fluctuations operating in the various directions are correlated with each other. However, little is known on the extent to which the instantaneous forces operating in the various three directions are correlated, nor it is known how the degree of correlation depends on frequency. Consequently, we make the simplifying assumption that the different forces applied in the different directions vary independently of each other. In that case, the terms associated with $i \neq j$ in equation 5 vanish and the PSD $P^g_{w_p}(f,\mathbf{x})$ becomes

$$P^g_{w_p}(f,\mathbf{x}) = 4\pi^2 f^2 \sum_{i=1}^{3} S^g_{F_i}(f,\mathbf{x}_0)G_{pi}(f,\mathbf{x};\mathbf{x}_0)^2, \quad (6)$$

where $S^g_{F_i}(f,\mathbf{x}_0) = \frac{\overline{[F_i(t,\mathbf{x}_0)]^2_f}}{df}$ is the PSD of the force time series $F_i(t,\mathbf{x}_0)$ acting on a given grain. The total PSD $P^T_{w_p}(f,\mathbf{x})$ resulting from the contribution of all river bed grains can be calculated by integrating the contribution of force time series $F_i(t,\mathbf{x}_0)$ over the full grain size distribution and the full length of river R as

$$P^T_{w_p}(f,\mathbf{x}) = \int_R \int_D 4\pi^2 f^2 \sum_{i=1}^{3} S_{F_i}(f,\mathbf{x}_0;D)G_{pi}(f,\mathbf{x};\mathbf{x}_0)^2 dD d\mathbf{x}_0, \quad (7)$$

where $S_{F_i}(f,\mathbf{x}_0;D)$ as the PSD of force time series per unit length and per unit D.

We proceed with our formulation for the PSDs $S^g_{F_i}$ and S_{F_i} for i equals 1, 2 and 3 by first calculating the PSD $S^g_{F_2}$ of the fluctuating drag forces, as an appropriate description of the instantaneous drag force timeseries exists on the basis of flow velocity timeseries (see equation 2). Then, we address the cases $i = 1$ and $i = 3$ by assuming that the PSD $S^g_{F_1}$ of the fluctuating lift forces and the PSD $S^g_{F_3}$ of the fluctuating cross-stream forces applied on a given grain are similar to the PSD $S^g_{F_2}$. This assumption is motivated by the fact that the frequency scaling of turbulent velocities is similar in any direction in the case of isotropic turbulence considered here [*Kolmogorov*, 1941] and that the force frequency scaling induced by these turbulent velocities is also expected to be similar in any direction. Moreover, in an unidirectional flow the downstream mean flow sets the production rate of turbulent kinetic energy through shear in the boundary layer, making turbulence in all three directions sensitive to the downstream velocity. The assumed direct correlation between the amplitude of lift and cross stream force fluctuations and the downstream velocity is supported by experiments performed on particles of various shapes immersed in a three dimensional turbulent flow advected at a given average velocity [*Vickery*, 1966; *Norberg*, 2003; *Naudascher and Rockwell*, 2005]. The assumption of similar amplitudes for $S^g_{F_1}$ and $S^g_{F_3}$ as compared to $S^g_{F_2}$ is also consistent with the measurements reported by *Schmeeckle et al.* [2007], where the amplitude of the lift force fluctuations was of the same order of magnitude as the drag force fluctuations. By considering $S^g_{F_1} = S^g_{F_3} = S^g_{F_2}$, we also assume for simplicity that the instantaneous lift and cross-stream coefficients C_L (denoted C_1 in the following) and C_C (denoted C_3 in the following) are equal to the instantaneous drag coefficient C_D (denoted C_2 in the following).

As the force history $F_2(t, \mathbf{x}_0)$ is governed by the instantaneous velocity timeseries $u_2(t, X_1)$ (see equation 2), we first calculate the PSD $S_{u_2}(f, X_1)$ of $u_2(t, X_1)$ (see section 2.1). Then, we use $S_{u_2}(f, X_1)$ to calculate the PSD $S^g_{F_2}(f, \mathbf{x}_0)$ (see section 2.2). Using $S^g_{F_1} = S^g_{F_3} = S^g_{F_2}$, we calculate the PSD S_{F_i} acting along all directions. Finally, after having derived the appropriate Green's function $G_{pi}(f, \mathbf{x}; \mathbf{x}_0)$ in section 2.3, we predict the ground power $P^T_{w_p}(f, \mathbf{x})$ by solving equation 7 (see section 2.4).

2.1. Velocity spectrum

In this section, we calculate the PSD of velocities that operates along the streamwise direction and upstream of a given grain. For simplicity and because of the lack of knowledge about the turbulent flow field within the bed roughness, we assume that the elevation X_1 at which $S_{u_2}(f, X_1)$ does not depend on the considered grain diameter D and we write $S_{u_2}(f, X^r_1) = S_{u_2}(f, X_1)$, where X^r_1 corresponds to a reference elevation within the bed roughness. Here, we set $X^r_1 = k_s/2$, where $k_s = 3D_{50}$ [*Kamphuis*, 1974] corresponds to the roughness size (see Figure 1), D_{50} being the median grain size. Under this rewriting, the velocity spectrum operating upstream of the different river bed grains depends on the roughness size, but is constant over the grain size distribution. The Reynolds decomposition of the instantaneous downstream velocity $u_2(t, X_1)$ operating at elevation $0 < X_1 \leq k_s$ above the bed (see Figure 1(b)), i.e. within the roughness layer, is introduced by writing $u_2(t, X_1) = \bar{u}_2(X_1) + u'_2(t, X_1)$, where $\bar{u}_2(X_1)$ is the average downstream velocity and $u'_2(t, X_1)$ is the fluctuating downstream velocity.

The depth variation of $\bar{u}_2$ in an open channel flow configuration is commonly described by a logarithmic profile [*Schlichting*, 1979]. However, most likely as a result of grain-induced form drag [*Wiberg and Smith*, 1991] and fluid deformation (i.e. eddy viscosity) associated with wakes shed by particles [*Lamb et al.*, 2008b], this logarithmic profile only poorly represents the average flow velocities within the bed roughness [*Nikora et al.*, 2001, 2004; *McLean and Nikora*, 2006]. Instead, the average velocity profile therein depends on the relative roughness k_s/H of the flow [*Bayazit*, 1976; *Tsujimoto*, 1991], and this dependence can be captured from scaling arguments between turbulence intensity and depth-averaged velocity [*Lamb et al.*, 2008b]. Following *Lamb et al.* [2008b], we describe the average downstream velocity profile within the bed roughness as

$$\bar{u}_2(X_1) \approx c_{\bar{u}}(X_1) u_*, \tag{8}$$

where $c_{\bar{u}}(X_1) = \frac{X_1}{0.12k_s}\left(1 - \left(\frac{X_1}{2k_s}\frac{k_s}{H}\right)\right)$ and u_* is the bed shear velocity.

Turbulence intensity, i.e. the root mean square (r.m.s.) of the fluctuating streamwise velocities $\sigma_{u_2}(X_1) = \sqrt{\overline{u_2(t,X_1)^2}}$, is also affected by particle roughness. Accordingly, $\sigma_{u_2}(X_1)$ exhibits a maximum value $\sigma_{u_2,max}$ near the top of the roughness layer, i.e. at $X_1 \approx k_s$ [*Raupach et al.*, 1991; *Nikora and Goring*, 2000; *Nezu and Rodi*, 1986]. The change in σ_{u_2} with decreasing elevation X_1 within the bed roughness is poorly known because turbulent velocity measurements are difficult to conduct there. Thus, for simplicity, we assume that σ_{u_2} does not depend on X_1 and we denote $\sigma_{u_2} = \sigma_{u_2}(X_1) = \sigma_{u_2,max}$ as well as $u_2'(t) = u_2'(t, X_1)$. Based on laboratory [*Bayazit*, 1976; *Wang et al.*, 1993; *Carollo et al.*, 2005] and field [*Nikora and Goring*, 2000; *Legleiter et al.*, 2007] measurements that report significant variations of $\sigma_{u_2,max}$ with relative roughness k_s/H, a dependence of σ_{u_2} with k_s/H is introduced following *Lamb et al.* [2008b] by approximating σ_{u_2} as

$$\sigma_{u_2} \approx c_\sigma u_*, \tag{9}$$

where $c_\sigma = 0.2\left[5.62\log_{10}\left(\frac{H}{k_s}\right) + 4\right]$.

The kinetic energy inherited from a mean flow characterized by a large Reynolds number (e.g. $>10^4$) is transferred to small scales by means of turbulent eddies [*Tennekes and Lumley*, 1972; *Nezu and Rodi*, 1986; *Venditti et al.*, 2013]. In rivers, the production of these turbulent eddies operates close to the river bed by the so-called bursting process [*Kline et al.*, 1967]. The formation of wall-layer streaks characterized by a succession of high and low flow speeds generates large shear stresses allowing burst-forming eddies [*Nakagawa and Nezu*, 1981; *Roy et al.*, 2004]. Following this picture, the production rate of turbulent kinetic energy associated with the generation of these eddies is set by the macroscopic shearing at the river bed. We assume that these eddies are typically formed at the reference elevation X_1^r, and the production rate of turbulent kinetic energy at this elevation is defined as

$$\wp(X_1^r) \equiv -\overline{u_1'(t)u_2'(t)}\Gamma_{12}(X_1^r), \tag{10}$$

where $\Gamma_{12}(X_1^r) = \frac{\partial \bar{u}_2(X_1^r)}{\partial X_1}$ is the macroscopic mean rate of strain and $\overline{u_1'(t)u_2'(t)}$ is the Reynolds stress [*Tennekes and Lumley*, 1972]. After having formed, these eddies are ejected above the bed roughness and eventually enlarge by coalescence as they are conveyed downstream by the average flow [*Yalin*, 1992]. As they become comparable in size to the flow depth, these eddies leave the productive range and enter the inertial subrange, where they break up into smaller eddies through a cascading process that allows the energy transfer towards smaller scales [*Kolmogorov*, 1941]. This transferred energy is dissipated at a spatial scale that is small enough such that viscous forces become important and the dissipation rate of turbulent kinetic energy operating at this spatial scale is defined as

$$\epsilon \equiv 2\nu\overline{\gamma_{ij}\gamma_{ij}}, \tag{11}$$

where ν is the kinematic viscosity and $\gamma_{ij} = \frac{\partial u_i'(t)}{\partial X_j}$ is the turbulent rate of strain [*Tennekes and Lumley*, 1972]. Assuming an idealized steady, homogeneous and pure shear open channel flow, the rates of turbulent production and dissipation at elevation X_1^r balance [*Tennekes and Lumley*, 1972] so that

$$\epsilon(X_1^r) = \wp(X_1^r). \tag{12}$$

By approximating the average velocity profile described in equation 8 as linear with depth, the mean rate of strain can be written

$$\Gamma_{12}(X_1^r) \approx \frac{\bar{u}_2(k_s)}{k_s} \approx c_{\bar{u}}(k_s)\frac{u_*}{k_s}, \tag{13}$$

where $\bar{u}_2(k_s)$ corresponds to the average downstream velocity at the top of the roughness layer. Moreover, based on previous measurments that report $\overline{u_1'(t)u_2'(t)}/(\sigma_{u_1}\sigma_{u_2}) \approx 0.5$ within the bed roughness [*Nezu and Nakagawa*, 1993], we approximate the Reynolds stress operating at X_1^r as

$$\sqrt{\overline{u_1(t)u_2(t)}} = \sqrt{\frac{\sigma_{u_1}\sigma_{u_2}}{2}} \approx \frac{c_\sigma u_*}{\sqrt{2}}, \tag{14}$$

where the assumption of isotropic turbulence has been done to approximate $\sigma_{u_1} = \sigma_{u_2} \approx c_\sigma u_*$ using equation 9. Substituting the expressions for the mean rate of strain (equation 13) and Reynolds stress (equation 14) into the production rate of equation 10, the turbulent dissipation $\epsilon(X_1^r)$ operating within the bed roughness can be approximated through equation 12 as

$$\epsilon(X_1^r) \approx \frac{c_{\bar{u}}(k_s)c_\sigma^2 u_*^3}{2k_s}. \tag{15}$$

The broad frequency range associated with the inertial subrange can be shown by substituting equation 15 into equation 11 and realizing that, given the characteristic Reynolds numbers $Re = UH/\nu \sim 10^4 - 10^5$ encountered in river flow, turbulent dissipation (governed by γ_{ij}) operates at much larger rates, i.e. frequencies, than turbulent production (governed by Γ_{12}). Each frequency band lying within these frequency limits corresponds to a single range of eddy sizes. *Kolmogorov* [1941] formalized the energy transfer through the intermediate scales of the inertial subrange, e.g. from the largest eddies to the smallest ones, and derived the famous "-5/3 law" for the energy spectrum. The nonnormalized Kolmogoroff spectrum E_{u_2} described in the wavenumber space k_w, at elevation X_1^r and in the downstream direction has the form

$$E_{u_2}(k_w, X_1^r) = K\epsilon(X_1^r)^{2/3}k_w^{-5/3} \tag{16}$$

where $K = 0.5$ is the Kolmogoroff universal constant [*Nezu and Nakagawa*, 1993]. By assuming that eddies of all sizes travel at the same downstream average velocity $\bar{u}_2(X_1^r)$, Taylor's frozen-turbulence hypothesis [*Taylor*, 1938] can be used to convert the PSD $E_{u_2}(k_w, X_1^r)$ of equation 16 expressed in the wavenumber space into the PSD $S_{u_2}(f, X_1^r)$ expressed in the frequency domain as

$$S_{u_2}(f, X_1^r) \approx \frac{2\pi}{\bar{u}_2(X_1^r)} E_{u_2}(k_w, X_1^r) = K\left(\frac{2\pi}{\bar{u}_2(X_1^r)}\right)^{-2/3} \epsilon(X_1^r)^{2/3} f^{-5/3} \tag{17}$$

where $f = 2\pi\bar{u}_2(X_1^r)/k_w$. Equation 17 holds within the inertial subrange, and the predicted -5/3 frequency scaling is an inherent feature of river flows, which has been widely observed in flume experiments and natural rivers [*Nezu and Nakagawa*, 1993].

The maximum frequency of the inertial subrange is set by the Kolmogorov microscale η_{Kolmo}, which is defined as the scale at which viscous forces become non-negligible. For typical Reynolds numbers associated with river flow, this upper bound frequency is on the order of $f_{max} \approx \bar{u}_2(X_1^r)/(2\pi\eta_{Kolmo}) \approx 10^3 - 10^5$ Hz [*Tennekes and Lumley*, 1972]. As f_{max} is orders of magnitude larger than the maximum seismic frequency of 10^2 Hz considered here, the tail end of the Kolmogorov energy spectrum does not affect the predictions and is consequently not modelled.

Within the roughness layer, the minimum frequency f_{min} of the inertial subrange is set by the macroscale there (also called the correlation length or mixing length), which we denote l_c [*Tennekes and Lumley*, 1972; *Nezu and Nakagawa*, 1993]. *Nikora et al.* [2001]; *Defina and Bixio* [2005] argue that l_c is dominated by wakes shed by particles within the bed roughness, and thus is set by the roughness size k_s (e.g., *Schlichting* [1979] proposed $l_c = 0.18k_s$, which has also been estimated in *Lamb et al.* [2008b]; *Wiberg and Smith* [1991] proposed $l_c = 0.41k_s$). Here, for simplicity, we assume $l_c \approx k_s$. Following *Tennekes and Lumley* [1972], we obtain $f_{min} \approx \bar{u}_2(X_1^r)/(2\pi k_s)$. For most rivers, f_{min} can be estimated to be roughly equal to 1 Hz. The truncation of the energy spectrum at f_{min} is introduced following *Tennekes and Lumley* [1972] and the PSD of flow velocities expressed in equation 17 can be rewritten in the full frequency range as

$$\begin{aligned} S_{u_2}(f, X_1^r) &\approx \tfrac{K}{3} k_s^{-\frac{2}{3}} \left[c_{\bar{u}}(X_1^r) c_{\bar{u}}(k_s) c_\sigma^2 \right]^{\frac{2}{3}} u_*^{8/3} f_{min}^{-5/3} \\ &\quad \times \left[1 - \tfrac{5}{11} \left(\tfrac{f}{f_{min}} \right)^2 \right] \quad \text{if} \quad f < f_{min} \\ S_{u_2}(f, X_1^r) &\approx \tfrac{K}{5} k_s^{-\frac{2}{3}} \left[c_{\bar{u}}(X_1^r) c_{\bar{u}}(k_s) c_\sigma^2 \right]^{\frac{2}{3}} u_*^{8/3} f^{-5/3} \quad \text{if} \quad f > f_{min}, \end{aligned} \tag{18}$$

where the formulation for the average flow velocity $\bar{u}(X_1^r)$ (equation 8) and turbulent dissipation $\epsilon(X_1^r)$ (equation 15) have been used. From this complete formulation for S_{u_2}, one can check that the integral of the Kolmogorov spectrum in the inertial subrange approaches the total energy, i.e. that we have

$$\int_{f_{min}}^{f_{max}} S_u^{x_1^r}(f, z_s) df \approx \sigma_{u_2}^2 \approx (c_\sigma u_*)^2. \tag{19}$$

Equation 18 does not incorporate the complex processes that operate within the productive range, where single/clustered burst eddies [*Nikora*, 2011] or large-scale flow structures [*Marquis and Roy*, 2013] form. These large structures, which have sizes that are typically on the order of several flow depths [*Venditti et al.*, 2013], operate at frequencies that are lower than f_{min}, i.e. lower than the frequency range of interest here. As a consequence, these coherent structures are not included in our analysis. Moreover, since we focus on $f > f_{min} \approx 1$ Hz in the seismic signal, our calculations performed in the following only consider the version of $S_{u_2}(f, X_1^r)$ that corresponds to $f > f_{min}$ in equation 18.

2.2. Force spectrum

Here, the PSD $S^g_{F_2}$ resulting from the fluctuating drag forces acting on a given river bed grain is calculated from the PSD S_{u_2} defined previously. Then, as discussed previously, $S_{F_1} = S_{F_3} = S_{F_2}$ is assumed so that all three force components can be included in our analysis. Finally, the PSD S_{F_i} of the force time series by unit length of river and unit grain size resulting from the sum of the force time series applied along direction i on each river bed grain of a given grain size distribution is calculated by integrating $S^g_{F_i}$ over a unit length of river and a unit grain size.

2.2.1. Calculation of $S^g_{F_2}$

The instantaneous total force applied on a given grain in equation 2 results from the spatial averaging of the instantaneous pressure differentials and shear stresses induced by the turbulent flow on subareas dA of A. We assume that the instantaneous stresses applied over these different subareas are only generated by the instantaneous velocities resulting from the free stream turbulence and impinging upon the grain. Therefore, we neglect the potential contribution of grain vibrations through vortex shedding and wake flapping [*Achenbach*, 1974; *Sarpkaya*, 1979; *Yuan and Michaelides*, 1992], which would result from velocity fluctuations occurring within the downstream wake of river bed grains.

The incorporation of these turbulent processes related to the dynamics of grain-wakes in the model would imply distinguishing them from the free stream turbulence. However, such a distinction is a difficult task within the bed roughness, since most of the grains lie within the downstream wake of other grains [*Schmeeckle and Nelson*, 2003]. Moreover, the characteristic scales for structures within the wakes behind particles are likely the same as those for the free stream turbulence in the roughness layer, namely u_* and D. Thus, by using the free stream turbulent flow field described in the previous section, we consider that the incremental fluctuating force $dF_i(t, X_1^{dA})$ operating on a subarea dA centered at elevation X_1^{dA} can be described similarly than in equation 2 from the instantaneous velocity $u_2(t, X_1^{dA})$ operating over that area. Thus, as done in *Naudascher and Rockwell* [2005], we rewrite equation 2 at the sub-grain scale as

$$\frac{dF_2(t, X_1^{dA})}{dA} = \frac{C_2 \rho_w}{2} \left[\bar{u}_2(X_1^{dA}) + u_2'(t, X_1^{dA}) \right]^2. \tag{20}$$

We also assume that the average velocity $\bar{u}_2(X_1^{dA})$ is constant over A and approximate this constant value by writing $\bar{u}_2(X_1^{dA}) \approx \bar{u}_2(X_1^r)$. From equation 20, we decompose the instantaneous force $dF_2(t, X_1^{dA})$ into an average force $d\bar{F}_2$ and a fluctuating force $dF_2'(t, X_1^{dA})$ as follow

$$\frac{dF_2(t, X_1^{dA})}{dA} = \frac{d\bar{F}_2(X_1^{dA})}{dA} + \frac{dF_2'(t, X_1^{dA})}{dA} \tag{21}$$

where

$$\frac{d\bar{F}_2(X_1^{dA})}{dA} \approx \frac{C_2 \rho_w}{2} \bar{u}_2(X_1^r)^2 \tag{22a}$$

$$\frac{dF_2'(t, X_1^{dA})}{dA} \approx C_2 \rho_w \bar{u}_2(X_1^r) u_2'(t, X_1^{dA}). \tag{22b}$$

The term of order $(u_2'(t, X_1^{dA})/\bar{u}_2(X_1^r))^2$ has been omitted in equation 22b because the amplitude of $u_2'(t, X_1^{dA})$ is of order $\sigma_{u_2,max}$, which implies that the ratio $(u_2'(t, X_1^{dA})/\bar{u}_2(X_1^r))^2$

is of order $[c_\sigma / c_{\bar{u}}(X_1^r)]^2$ (using equations 8 and 9). For the typical relative roughness values of $H/k_s \approx 1 - 10$, we obtain $(u_2'(t, X_1^{dA})/\bar{u}_2(X_1^r))^2 \sim 10^{-1}$, and the terms of order $(u_2'(t, X_1^{dA})/\bar{u}_2(X_1^r))^2$ can thus be neglected. Following *Naudascher and Rockwell* [2005], the mean square contribution of the fluctuating stress time series $\frac{dF_i'(t, X_1^{dA^a})}{dA^a}$ and $\frac{dF_i'(t, X_1^{dA^b})}{dA^b}$ acting at two different locations a and b of A can be defined in the frequency domain by the cospectral density

$$\Sigma_2^{ab}(f; D) \equiv \frac{\overline{\left[\frac{dF_2'(t, X_1^{dA^a})}{dA^a} \frac{dF_2'(t, X_1^{dA^b})}{dA^b}\right]_f}}{df}, \tag{23}$$

and the resulting PSD $S_{F_2}^g(f; D)$ applied on A is defined as

$$S_{F_2}^g(f; D) \equiv \iint_A \Sigma_2^{ab}(f; D) dA^a dA^b. \tag{24}$$

By using the decomposition of forces formulated in equations 21 and 22 to express $\frac{dF_2'(t, X_1^{dA^a})}{dA^a}$ and $\frac{dF_2'(t, X_1^{dA^b})}{dA^b}$ in equation 23, we can write

$$\Sigma_2^{ab}(f) \approx \Big(C_2 \rho_w \bar{u}_2(X_1^r)\Big)^2 S_{ab}^g(f), \tag{25}$$

where $S_{ab}^g(f) = \frac{\overline{\left[u_2'(t, X_1^{dA^a}) u_2'(t, X_1^{dA^b})\right]_f}}{df}$. By substituting equation 25 into equation 24, we obtain

$$S_{F_2}^g(f; D) \approx \Big(C_D \rho_w \bar{u}_2(X_1^r) A\Big)^2 \frac{1}{A^2} \iint_A S_{ab}^g(f) dA^a dA^b. \tag{26}$$

Finally, following the assumption that $S_{F_1} = S_{F_3} = S_{F_2}$ and substituting the PSD $S_{u_2}(f, X_1^r)$ defined in the previous section into equation 26 through defining the function $\chi_{fl}(f; D)^2 = \frac{1}{A^2} \iint_A \frac{S_{ab}^g(f)}{S_{u_2}(f, X_1^r)} dA^a dA^b$, the PSD of force fluctuations obtained in equation 26 can be rewritten for force fluctuations operating in any direction i as

$$S_{F_i}^g(f; D) \approx \Big(C \rho_w \bar{u}_2(X_1^r) A\Big)^2 S_{u_2}(f, X_1^r) \chi_{fl}(f; D)^2, \tag{27}$$

where $C = C_1 = C_3 = C_2$. Equation 27 states that the energy of the fluctuating force applied over the entire area A, which results from the summation of all the fluctuating forces applied on the subareas dA, is proportional to the average downstream velocity. In addition, at a given frequency f, the resultant fluctuating force amplitude is lessened by a normalization factor $\chi_{fl}(f;D)^2 \leq 1$, where $\chi_{fl}(f;D)^2$ expresses the capability of a river bed grain to convert velocity fluctuations into force fluctuations. The larger the eddy size is with respect to the area A, the more similar time variations of $u'_2(t, X_1^{dA^a})$ and $u'_2(t, X_1^{dA^b})$ are, and thus the greater is $S^g_{ab}(f)$. The smaller the eddy sizes, the more likely the total force resulting from the fluctuating velocities operating at the different places of the grain surface cancel with each other. These features are related to the fluid-dynamic admittance of a given rigid surface, and have been constrained from previous experiments and theoretical developments for various surface shapes. Following *Naudascher and Rockwell* [2005], we use an empirical formulation based on experimental tests conducted on plates of various geometries to formulate $\chi_{fl}(f;D)$ as

$$\chi_{fl}(f;D) = \frac{1}{1 + \left[\frac{2f}{f_c(D)}\right]^{4/3}}, \tag{28}$$

where $f_c(D) \equiv \bar{u}_2(x_2^r)/D$.

2.2.2. Calculation of S_{F_i}

The resultant force applied on the full width and on a unit length of river corresponds to the spatial average of all forces applied on each river bed grain. In order to sum up all contributions, we assume that the force time series are randomly spaced in time from one grain to another. Such a behavior is expected for grain sizes of the order or larger than the bed roughness size k_s where, in that case, the grains are separated by a distance larger than the correlation length $l_c \approx k_s$ considered for the turbulent flow. For smaller grains, the assumption of a random time spacing of force time series from one grain to another is less appropriate, as the turbulent flow velocities are expected to be correlated up to spatial scales that are larger than a single grain size. However, in practice, the turbulent flow field within the bed roughness may be dominated by the downstream wakes of the particles, causing values of l_c to be of the order of the grain diameter D located upstream of the considered grain [*Schmeeckle and Nelson*, 2003]. The incorporation of these spatial variations of l_c in the present model would imply assumptions of grain packing geometries within the bed roughness, which would add considerable complexity. Thus, in order to keep the model as simple as possible, we assume the independence of force time series from grain to grain. Under this assumption, the sum of force time series does not affect the shape of the spectrum defined in equation 27 and the PSD $S_{F_i}(f, \mathbf{x}_0)$ of the resultant force time series can be written as

$$S_{F_i}(f, \mathbf{x}_0; D) = N_g(D) \cdot S^g_{F_i}(f, \mathbf{x}_0; D), \tag{29}$$

where $N_g(D)$ is the number of grains for a unit length of river and a unit grain size.

Following *Tsai et al.* [2012], $N_g(D)$ is calculated using the log-'raised cosine' grain size distribution $p(D)$. The log-'raised cosine' distribution is analogous to a log-normal distribution except that it includes a cut-off at both large and small D. Assuming that the grain assembly at the river bed exhibits a packing fraction slightly smaller than 1, the number of grains of size D for a unit length of river and a unit grain size can be approximated as

$$N_g(D) \approx \frac{p(D) \cdot W}{D^2}, \tag{30}$$

where W stands for the river width.

By substituting the expression of the PSD $S^g_{F_i}(f)$ of forces applied on a single grain (equation 27) and the formulation of the number of river-bed grains $N_g(D)$ (equation 30) into the PSD $S_{F_i}(f, \mathbf{x}_0; D)$ of force time series applied on all grains over a unit length and a unit grain size of river (equation 29), $S_{F_i}(f, \mathbf{x}_0; D)$ can be approximated as

$$S_{F_i}(f, \mathbf{x}_0; D) \approx \frac{3}{5} W p(D) D^2 \rho_w^2 c_{\bar{u}}(X_1^r)^2 C^2 u_*^2 S_{u_2}(f, X_1^r) \chi_{fl}(f; D)^2, \tag{31}$$

where equation 8 has been used to formulate the average velocity $\bar{u}_2(X_1^r)$. By substituting the expression of $S_{u_2}(f, X_1^r)$ obtained in the previous section (see equation 18) into equation 32, we write the final expression of $S_{F_i}(f, \mathbf{x}_0; D)$ as

$$S_{F_i}(f, \mathbf{x}_0; D) \approx \frac{K}{8} \frac{W p(D) D^2}{k_s^{2/3}} \rho_w^2 C^2 \zeta(H/k_s) u_*^{14/3} f^{-5/3} \chi_{fl}(f; D)^2, \tag{32}$$

where $\zeta(H/k_s) = \left[c_{\bar{u}}(k_s)^{1/3} c_{\bar{u}}(X_1^r)^{4/3} c_\sigma^{2/3}\right]^2$.

2.3. Green's function

As stated in the beginning of this model section, a single component p of ground motion is potentially affected by all of the three force fluctuation components. More precisely, the horizontal (direction 2) and lateral (direction 3) components of forces, i.e. the forces that operate along the Earth's surface plane, generate Love waves, while all the three components (i.e. horizontal, lateral and vertical) of forces generate Rayleigh waves. Assuming that the local topographic slope of the river banks on which the seismic station is deployed is small, the vertical component of the seismic station is only affected by Rayleigh waves. On the other hand, the broad spatial distribution of turbulent flow noise sources operating all along the river implies both horizontal components of the seismic station to be a combination of both Rayleigh and Love waves. In order to avoid accounting for both Rayleigh and Love waves and separating their contributions, we here only focus on the vertical component of the seismometer and we calculate $P^T_{w_1}(f, \mathbf{x}; D)$ from equation 7, where index 1 indicates the vertical direction (see Figure 1). The amplitude of the Green's function components $G_{1i}(f, \mathbf{x}; \mathbf{x}_0)$ for vertical ground motion caused by an impulse force applied in the i^{th} direction can be calculated for the fundamental mode following *Aki and Richards* [2002] as

$$\begin{vmatrix} G_{11} \\ G_{12} \\ G_{13} \end{vmatrix} = \frac{1}{8 v_c v_u I_1} \begin{pmatrix} r_1(z_F) r_1(z_S) \\ r_1(z_F) r_2(z_S) \cos\varphi \\ r_1(z_F) r_2(z_S) \sin\varphi \end{pmatrix} \sqrt{\frac{2}{\pi k r}} e^{-\pi f r/(v_u Q)} \tag{33}$$

where $k = 2\pi f / v_c$ is the angular wavenumber of the Rayleigh wave, v_c is the phase velocity, v_u is the group velocity, $r = |\mathbf{x} - \mathbf{x}_0|$ is the source-station distance, φ is the azimuth, Q is the (dimensionless) quality factor, r_1 and r_2 are the vertical and horizontal Rayleigh wave eigenfunctions, z_F and z_S are the depths of the point source and the seismic station, respectively, and I_1 is defined as follows

$$I_1 = \frac{1}{2} \int_0^\infty \rho_s (r_1^2 + r_2^2) dz, \tag{34}$$

where ρ_s is rock density. As the seismic wavelengths of interest are much larger than the source depth $z_F \approx H$, we can approximate $z_F = z_S \approx 0$. Assuming constant density with depth, the coefficients $r_1(0)$, $r_2(0)$ and I_1 as well as the surface wave velocities $v_c(f)$ and $v_u(f)$ are described by *Tsai and Atiganyanun* [2014], who performed numerical computations to reconstruct the Green's function of Rayleigh waves from shear velocity depth-profiles. Using the shear velocity profile given by *Boore and Joyner* [1997] for a generic rock site, i.e. assuming a shear velocity depth profile described by a power law of the form

$$v_s(z) = v_0 (z/z_0)^\alpha \tag{35}$$

where $z_0 = 1000$ m and v_0 and α are constants that are given at various depth ranges in *Boore and Joyner* [1997], we approximate from *Tsai and Atiganyanun* [2014] that

$$\begin{aligned} r_1(0)r_1(0)/I_1 &\approx 0.6k \\ r_1(0)r_2(0)/I_1 &\approx 0.8k. \end{aligned} \tag{36}$$

These expressions imply a horizontal to vertical ratio, i.e. $r_2(0)/r_1(0)$-ratio, of the order of 1.3, which roughly corresponds to that modelled in *Bonnefoy-Claudet et al.* [2006] as well as that measured on river banks (Gimbert et al., Using seismic observations to quantify river mechanics: example of the "Les Bossons" river (France), *In prep.*) in a similar frequency range. By replacing these expressions in equation 33, the final expression for the amplitude of the Green's function is approximated as

$$\begin{vmatrix} G_{11} \\ G_{12} \\ G_{13} \end{vmatrix} \approx \frac{k}{8\rho_s v_c v_u} \begin{bmatrix} 0.6 \\ 0.8\cos\varphi \\ 0.8\sin\varphi \end{bmatrix} \times \sqrt{\frac{2}{\pi k r}} e^{-\pi f r/(v_u Q)}. \tag{37}$$

Also from *Tsai and Atiganyanun* [2014], we describe the Rayleigh wave phase and group velocities v_c and v_u as

$$\begin{aligned} v_c(f) &= v_{c0}(f/f_0)^{-\xi} \\ v_u(f) &= v_c(f)/(1+\xi) \end{aligned} \tag{38}$$

where $f_0 = 1$ Hz, and ν_{c0} and ξ are constants. As the comparison of model predictions with available data is mostly done between 1 and 10 Hz, we use $\nu_{c0} = 2175$ m/s and $\xi = 0.48$ as reasonable values in that range. Finally, following *Erickson and Mcnamara* [2004], the quality factor Q is modeled in the form of

$$Q = Q_0(f/f_0)^{\eta}, \tag{39}$$

where Q_0 and η are constant parameters. As in *Tsai et al.* [2012] and following the suggestions of *Anderson and Hough* [1984], we consider $Q_0 = 20$ and $\eta = 0$.

2.4. Final model formulation

In order to obtain our final model, the average shear velocity at the average bed elevation is written assuming a steady and uniform flow (when averaged over turbulence) as

$$u_* = \sqrt{gH \sin\theta}, \tag{40}$$

where g is the gravitational constant and θ is the channel slope angle. *Schmeeckle et al.* [2007] measured typical values of C_2 (i.e. instantaneous drag coefficients) in flume experiments and reported values increasing from 0.4 to 1.6 as the average downstream velocity is decreased. Here, for simplicity, we do not account for a dependence of C with the average downstream velocity, and we set $C = 0.5$. Also, as the PSDs of force fluctuations are assumed similar in all directions i, we denote $S_F = S_{F_i}$.

By substituting the expression for the Green's function provided in equation 37 (and using the definitions of the wave propagation parameters provided in equations 38 and 39) into the total expression of the predicted seismic power recorded at a given station (equation 7), we approximate $P^T_{w_1}(f, \mathbf{x})$ as

$$P^T_{w_1}(f, \mathbf{x}) \approx 4\pi^2 f^2 \int_R \left[\int_D S_F(f, \mathbf{x}_0; D) dD \right] \cdot \left(\frac{k}{8\rho_s v_c v_u} \right)^2 \frac{2}{\pi k r} e^{-2\pi f r/(v_u Q)} dr. \tag{41}$$

The total PSD of ground motion recorded at $\mathbf{x}$ is obtained by substituting equation 32 for the force spectrum S_F into equation 41. We therefore obtain

$$P^T_{w_1}(f) \approx \frac{KW}{3k_s^{2/3}} \left(\frac{\rho_w}{\rho_s} \right)^2 \frac{(1+\xi)^2}{f_0^{5\xi} v_{c0}^5} \cdot \zeta(H/k_s) \cdot \psi_\beta(f) \cdot \phi_D(f) \\ f^{4/3+5\xi} \cdot g^{7/3} \sin(\theta)^{7/3} \cdot C^2 H^{7/3} \tag{42}$$

where

$$\begin{cases} \phi_D(f) = \int_D p(D) D^2 \chi_{fl}(f; D)^2 dD \\ \psi_\beta(f) = \int_R \frac{1}{r} e^{-\beta r} dr \end{cases} \tag{43}$$

and

$$\beta = 2\pi r_0(1+\xi)f^{1+\xi-\eta}/(v_{c0}Q_0 f_0^{\xi-\eta}). \quad (44)$$

As in *Tsai et al.* [2012], $\psi_\beta(f)$ can be approximated analytically by assuming an infinitely long and straight river whose closest point in the horizontal Earth's surface plane is r_0 from the seismic station and writing

$$\psi_\beta(f) = \int_{-\infty}^{\infty} \frac{1}{\sqrt{1+y^2}} \exp(-\beta\sqrt{1+y^2})dy$$
$$\approx 2\log\left(1+\frac{1}{\beta}\right)e^{-2\beta} + (1-e^{-\beta})e^{-\beta}\sqrt{\frac{2\pi}{\beta}}. \quad (45)$$

The strong scaling of $P_{w_1}^T$ with H (to the 7/3 power) in equation 42 shows that seismic observations are strongly set by water flow depth. This also implies a strong scaling with u_* (see equation 40), such that seismic observations ($P_{w_1}^T$) can be used to invert for u_* and H. A quantitative evaluation of the model is performed in section 4 against the observations reported by *Schmandt et al.* [2013] in the Colorado river, USA. Prior to this, the features of equation 42 are discussed, and qualitative comparisons are performed with the observations reported by *Burtin et al.* [2008] at the Trisuli river, Nepal.

3. Model results

Here, we provide a general view on the behavior of model predictions with varying model parameters. Moreover, the turbulent flow model predictions are compared with the ones obtained for a bedload source using the model proposed by *Tsai et al.* [2012], who derived the PSD $P_{b_1}^T$ of vertical ground velocities resulting from a sediment flux q_b transported as bedload. Similar to *Tsai et al.* [2012], we apply our model predictions to the Trisuli river, for which *Burtin et al.* [2008] reported seismic noise acquisitions. The river geometry is described using the same parameters as used in *Tsai et al.* [2012]: we use $W = 50$ m for channel width, $\theta = 1.4°$ for river slope angle, $D_{50} = 0.15$ m for the median size of river bed grains and $\sigma_g = 0.52$, where σ_g is the standard deviation of the log-'raised cosine' distribution $p(D)$ of river bed grains. Numerical simulations performed recently by *Tsai and Atiganyanun* [2014] provide a more realistic description of the Rayleigh wave propagation compared with using the approximations made in *Tsai et al.* [2012]. Consequently, the parameters used here to describe the Rayleigh wave propagation are slightly different than in *Tsai et al.* [2012]. Phase and group velocities v_c and v_u are calculated using $v_{c0} = 2175$ m/s and $\xi = 0.48$ in equation 38 (instead of the values of $v_{c0} = 1295$ m/s and $\xi = 0.374$ used in *Tsai et al.* [2012]), and the prefactor used to describe the vertical component of the Green's function associated with a vertical force ($|G_{11}|$ in equation 37) is equal to 0.6, instead of the value of 1 considered in *Tsai et al.* [2012]. We describe the quality factor Q_0 (which quantifies anelastic attenuation) similarly to *Tsai et al.* [2012], i.e. we use $Q_0 = 20$, $f_0 = 1$ Hz and $\eta = 0$ in equation 39, and set the river-to-station distance to $r_0 = 600$ m so it roughly corresponds to the seismic deployments considered by *Burtin et al.* [2008]. Finally, we take $H = 4$ m as water flow depth, as well as $q_b = 0.045$ m^2/s for the associated bedload flux. This value of q_b is within the range of values inferred by *Tsai et al.* [2012]. These default parameters are listed in Table 3.

3.1. Predictions for the Trisuli river using default model parameters

Turbulent flow and bedload model PSDs are shown as a function of frequency in Figure 2(a) using the default Trisuli parameters listed in Table 3. The maximum ground power obtained without tuning any model parameters from the turbulent flow noise model corresponds to -135.5 dB, which is of the same order of magnitude as the maximum PSDs reported in *Burtin et al.* [2008]. Thus, our model predicts that turbulent flow plays a significant role in the PSDs reported by *Burtin et al.* [2008]. In addition, while accounting for turbulent flow noise introduces larger energy at lower frequencies in the total PSDs as compared to the PSD modelled using *Tsai et al.* [2012], the combination of our model with the bedload model of *Tsai et al.* [2012] remains consistent with the general aspect of the observations reported by *Burtin et al.* [2008]. A single peak occurs around $\approx 6-7$ Hz, whereas a sharper energy increase operates at low frequencies, in contrast to the gradual decrease at high frequencies. The similarities between the turbulent flow and bedload predictions shown here explain the difficulties encountered by *Burtin et al.* [2008] to extract a clear water-flow-induced signal from the observed PSDs. Based on these model predictions, we suggest that the hysteresis reported over the broad $3-15$ Hz frequency range by *Burtin et al.* [2008] must differ when investigating different frequency ranges. In particular, we expect a more pronounced hysteresis at larger frequencies, where bedload-induced-noise is predicted to dominate over water-flow-induced-noise.

The relative contribution of turbulent flow versus bedload in the total PSD is, however, drastically modified when varying the distance r_0 between the seismic station and the channel. Using $r_0 = 100$ m as an example (see Figure 2(b)), the bedload-induced-noise dominates most frequencies, while the peak frequencies f_w^{peak} and f_b^{peak} associated with maximum turbulent flow and bedload model PSDs are more separated from each other. The following sections discuss in detail the role of model parameters in modifying f_w^{peak} and $P_{w_1}^T(f_w^{peak})$, in particular with respect to f_b^{peak} and $P_{b_1}^T(f_b^{peak})$.

3.2. Sensivity of the Peak Frequency on model parameters

The functions $\psi_\beta(f)$ and $\phi_D(f)$ of equation 42 control variations of the predicted frequency scaling with model parameters. The function $\psi_\beta(f)$ accounts for the modulation of the source spectrum as surface waves travel into the ground, which is set by the river-to-station distance r_0 and the value of the quality factor Q_0 (for a given ground depth-profile of shear wave velocities). The surface wave path effect accounted for by $\psi_\beta(f)$ is similar to that accounted for by *Tsai et al.* [2012] in the bedload model. As the attenuation of Rayleigh waves preferentially damps larger frequencies (see also equation 37), f_w^{peak} is predicted to decrease as r_0 increases or Q_0 decreases (see Figure 2 and Figure 3(a)). Superimposed on this wave path effect, the function $\phi_D(f)$ that converts turbulent velocities into force fluctuations acting on each river-bed grain modifies the values of f_w^{peak} by adding, at frequencies larger than $f_c = \bar{u}_2(X_1^r)/D$, a -8/3 slope decrease (see equation 28) to the -5/3 Kolmogorov frequency scaling (see equation 18). For a given river slope and a given bed grain size distribution, the value of f_c at which this modification occurs only depends on the river bed roughness H/k_s (see equation 8). The larger the ratio H/k_s, the larger the cut-off frequency of function χ_{fl}, and thus the larger f_w^{peak} is (see Figure 3(a)). However, for a given site at which H/k_s-values typically vary from a factor of 2 to 4, the associated changes predicted in f_w^{peak}-values are weak. This weak dependence of f_w^{peak} on H/k_s is in agreement with previous observations [*Burtin et al.*, 2008; *Schmandt et al.*, 2013], which report no significant shift in central frequency with varying water discharge.

To compare variations of f_w^{peak} with f_b^{peak}, we approximate f_b^{peak} analytically from *Tsai et al.* [2012] as $f_b^{peak} \approx [4.9Q_0 v_{c0}(1+\xi) f_0^{0.4}/(2.8\pi r_0)]^{1/1.4}$. In agreement with previous observations [*Burtin et al.*, 2011; *Schmandt et al.*, 2013], the negative scaling of the turbulent flow source function with frequency (while the bedload source is constant) causes

f_w^{peak}/f_b^{peak} to consistently be lower than 1 (independent of H/k_s and r_0, see Figure 3(b)), i.e. the water-flow induced noise is predicted to always operate at lower frequencies than the bedload-induced noise. In addition, smaller anelastic attenuation of surface waves, i.e. either smaller values of r_0 or larger values of Q_0, causes the higher frequency part of the source spectrum to more strongly contribute to the ground velocity PSD. As the turbulent flow spectrum shows a larger decrease with frequency at these higher frequencies, a slower decrease of f_w^{peak} as compared to f_b^{peak} occurs as r_0 increases or Q_0 decreases, implying the frequency range of the turbulent-flow-induced noise to differ more than the bedload one in these cases. This explains the capability of *Burtin et al.* [2011] and *Schmandt et al.* [2013] to isolate the seismic signature of water-flow-noise by deploying seismic stations close to the river (e.g., values of $r_0 \approx$ 10-50 m have typically been considered in these studies).

3.3. Sensitivity of PSD Amplitude on model parameters

Here, the amplitude of model PSDs (see equation 42) is discussed as a function of grain diameter D (through ϕ_D), roughness of the flow H/k_s (through ζ), river-to-station distance r_0 and ground quality factor Q_0 (through ψ_β), river slope angle θ and flow depth H.

The amplitude of model predictions resulting from the grain size distribution is shown in Figure 4, in which $P_{w_1}(f_w^{peak}; D)$ is compared with $P_{b_1}(f_b^{peak}; D)$, where $P_{x_1}(f_x^{peak}; D)$ (x either stands for w or b) is defined such that $P_{x_1}^T(f) = \int_D P_{x_1}(f; D)dD$. The peak noise predicted at $D = 0.18$ m (corresponding to D_{58}, i.e. the 58th percentile grain size) for the turbulent flow model occurs at a much smaller grain size than the grain size associated with maximum $P_{b_1}^T(f_b^{peak}; D)$ (corresponding to D_{94} [*Tsai et al.*, 2012]). While slightly affected by variations in the standard deviation σ_g of the grain size distribution, the dominant grain size is always larger than the median grain size D_{50} (see Figure 4(b)) and remains significantly smaller than the one that dominates bedload seismic noise. Thus, as compared to the bedload model predictions, an accurate knowledge of the end-tail of the grain size distribution is less critical to obtain realistic estimates of the noise induced by turbulent flow. A log-normal distribution could be used instead of the log-'raised cosine' function considered here, which was originally introduced by *Tsai et al.* [2012] to avoid the disproportional and unrealistic contribution of large grains when transported as bedload. For the median grain size of $D_{50} = 0.15$ m, we can see on Figure 4 that turbulent flow induced noise is predicted to be of the order of the bedload induced noise. Modifications of this picture with varying median grain sizes D_{50}, i.e. roughness scale k_s, is shown at constant water flow depth $H = 4$ m and as a function of r_0 on Figure 5.

The turbulent flow induced noise is compared with the bedload one for varying median grain sizes D_{50} by calculating $P_{b_1}(f_b^{peak}; D)$ using a bedload flux q_b that is scaled with the bedload flux at transport capacity q_{bc}, where q_{bc} is calculated following *Fernandez Luque and Van Beek* [1976] as

$$q_{bc} = 5.7\sqrt{RgD_{50}^3}(\tau_* - \tau_{*c})^{3/2}, \tag{46}$$

with $R = (\rho_s - \rho_f)/\rho_f$, $\tau_* \equiv u_*^2/(RgD)$, $\tau_{*c} = \tau_{*c50}(D/D_{50})^{-\gamma}$ and $\gamma \approx 0.9$ [*Parker*, 1990]. In contrast to the bedload source, where smaller D_{50}-values cause lower seismic noise as a result of less energy released at each grain impact (see Figure 5(b)), the increasing average and turbulent flow velocities associated with smaller D_{50}-values (see equations 8 and 9) result in larger turbulent flow induced noise (as shown on Figure 5(a) at small values of r_0). However, as r_0 is larger and/or Q_0 is smaller, this picture is modified by a wave propagation effect. Far away from the river channel, e.g., say $r_0 = 600$ m, $P_{w_1}^T$ shows the unintuitive behavior of decreasing $P^T_{w_1}$ with increasing H/k_s-values for deep flows. This behavior is explained by the fact that, for stronger Rayleigh wave attenuation (either from larger Q_0-values or larger r_0-values), the low frequency content of the source PSD S_F contributes more into the maximum value of $P^T_{w_1}$ predicted. Because of the less drastic decrease of S_F with frequency in this lower frequency range ($f < f_c$ for most grains in that case, see equation 32 and the associated χ_{fl}-dependence), $P^T_{w_1}$ decreases faster with r_0, and eventually becomes lower for deep flows than shallow flows for large enough r_0-values. Such an unintuitive behavior is not observed for bedload, as the contact-time impact assumed to be smaller than the sampling time of the seismic station causes the bedload source spectrum to not depend on frequency [*Tsai et al.*, 2012]. Finally, also because the PSD S_F decreases with frequency while the bedload source does not, one can notice that the migration of the signal toward lower frequencies at increasing distance from the river causes a faster decrease of the amplitude of bedload induced noise with respect to turbulent flow induced noise.

The different variations of $P^T_{w_1}$ and $P^T_{b_1}$ with r_0, H/k_s and Q_0 imply that the relative contribution of seismic noise induced by turbulent flow versus seismic noise induced by bedload varies drastically for different flows and seismic deployment configurations (see Figure 6). Assuming that bedload transport evolves in proportion to bedload transport capacity, seismic noise signal is dominated by water flow at large river-to-station distances and large values of H/k_s, while bedload dominates for seismic noise recorded closer to the seismic station and for smaller H/k_s-values. Notably, for a given site (i.e. given values of H/k_s and given ground seismic properties), turbulent flow and bedload can be characterized independently by evaluating seismic noise at various distances from the river. There also exists a relatively narrow range of H/k_s and r_0-values for which both turbulent flow and bedload exhibit significant amplitudes and different enough frequency ranges such that they can be distinguished from a single record (range delimited by the dashed lines on Figure 6, see section 4 for such a configuration in the case of the Hance Rapids section at the Colorado River). In this range where turbulent flow induced noise can be isolated from the seismic signal (materialized by the blue areas on Figure 6), the modelling framework presented here can allow inverting for bed shear velocity u_* directly from the equation 32 of the model, or for water flow depth H through equation 40. The direct scaling of ground power resulting from turbulent flow induced noise with shear velocity u_* or water flow depth H ensures that good constraints can be obtained on these parameters from seismic data, as long as ground motion is evaluated far enough from the river (see Figure 7). When evaluating ground motion closer to the river channel, one needs larger values of u_* in order to be able to distinguish the turbulent flow signature with respect to the bedload signature and thus invert for u_* or H.

The position at which these transitions between turbulent flow and bedload dominated noise occur (i.e. position of the dashed lines on Figure 6 and Figure 7) is also modified by the river bed slope angle θ. Assuming that bedload transport evolves in proportion to transport capacity for varying values of θ, Figure 8(a) shows that bedload induced noise dominates at lower slopes. In contrast, the stronger increase of turbulent flow induced noise with increasing river slope angle θ results in predominant turbulent flow induced noise conditions at steeper slopes. Thus, steeper slopes would cause the dashed lines of Figure 6 and Figure 7 to shift toward the left side of the diagrams, i.e. toward smaller

r_0-values. As a consequence, a larger range of u_* or H-values can be inverted for these steeper cases.

Finally, in the perspective of inverting u_* or H from the seismic signal along varying discharge events, we can see on Figure 8(b) that the differential increase of $P^T_{w_1}$ with increasing H is larger for smaller initial H_0/k_s-values, where H_0 stands for a reference depth. In other words, a similar increase in H results in a larger increase in $P^T_{w_1}$ for shallow compared to deeper river flows. In addition, it is interesting to note that, as bedload transport evolves in proportion to transport capacity for varying river flow depth H, the bedload induced noise increases considerably slower with H as compared to the turbulent flow induced noise.

4. Model application to "Hance Rapids" (Colorado River, USA)

In this section, we quantitatively compare our model predictions to the field seismic observations reported at "Hance Rapids" (HR) in the Colorado river [*Schmandt et al.*, 2013]. We judge that, to date, only the HR dataset provides a clear seismic signature of turbulent flow noise as well as sufficient information on river geometry and hydrological parameters to make a meaningful model comparison. For other datasets, either a water-flow-induced signal has not been clearly identified by the authors, as for the Trisuli (Himalaya) and Cho-Shui (Taiwan) rivers [*Burtin et al.*, 2008; *Hsu et al.*, 2011], or the hydrological conditions in the river channel at the location of the seismic stations were unknown, as in *Burtin et al.* [2011] where flow depth was only measured at the downstream end of the river, while several channels may have operated during the time of record, all potentially with different and non-documented local channel widths and depths.

Schmandt et al. [2013] reported seismic observations acquired during a controlled flood experiment associated with three main components in the seismic signal (see Figure 3 of *Schmandt et al.* [2013]). Two of these 3 components, with low-frequency peaks located between 0.5 and 10 Hz, were attributed to water flow induced noise, as no hysteresis behavior could be observed with respect to river discharge at these frequencies. The third component, observed at higher frequencies (between 15 and 45 Hz), was identified as bedload, as the signal in this frequency range is characterized by a strong temporal intermittency and hysteresis relative to water level. At frequencies lower than 10 Hz, the authors suggested that the relatively high frequency peak centered around 6-7 Hz resulted from the breaking of waves occurring at the fluid air interface, as large infrasound energy was also observed in the same frequency range. In contrast, the low frequency peak occurring at several seconds of period (centered around 0.7 Hz) was proposed to result from fluid forces operating on the rough river bed. In this context, we here apply our physical model in order to determine whether some of these spectral features can be captured. Prior to performing model predictions, we introduce the river geometry and fluvial parameters, as well as ground seismic properties.

4.1. River parameters

The geometry of the river and its fluvial properties are inferred from the direct measurements provided by the US Geological Survey [*Kieffer*, 1988, 1987]. Although the measurements reported therein were conducted more than 20 years before the seismic acquisitions of *Schmandt et al.* [2013], we assume that they still provide reasonable estimates of the current rapids configuration. This assumption is supported by the relative stability of the river bed geometry there, as the river bed is mainly made of big boulders anchored in the main stream and are not mobilized by the usual discharges reached in the Colorado river.

4.1.1. Channel Geometry

The river bed slope angle θ is obtained from the water surface elevations provided in *Kieffer* [1988]. We estimate a river slope angle of about $\theta \approx 1^o$ over the 150 m of the rapids section.

Over the rapids section, the channel width W varies from about 80 to 100 m for the various discharges (see Figure 9(a)). As W does not play a key role in the model predictions, we take W to be constant with discharge. We set $W = 90$ m for $Q_w > 140$ m^3/s (see Figure 10).

The cross stream topography is set from the cross section transect X-X' provided in *Kieffer* [1988] and shown in Figure 9(a). We assume that the cross-section X-X' is representative of the reach. Based on *Kieffer* [1988], three subsections are defined with respect to a base water level where $Q_w = 140$m^3/s (see Figure 10(a)). Subsection 1 is 20 m wide and has negligible flow velocities due to the fairly large and densely arranged boulders in that region. As a consequence, no flow is modelled in that region for $Q_w = 140$m^3/s, while only the excess water flow depth is accounted at larger discharges. Subsection 2 is 30 m wide and has an average depth of 1.64 m. Subsection 3 is 30 m wide and has an average flow depth of about 0.9 m.

The boulder size distribution is reported on Figure 9(b) from the measurements of *Kieffer* [1987], which were taken in the debris fan located downstream of Red Canyon (shown by the red rectangle in Figure 9(a)). We assume that these measurements are representative of the rapids section and the 'log'-raised cosine distribution $p(D)$ is adjusted using $D_{50} = 0.5$ m and $\sigma_g = 0.7$, resulting in $k_s = 1.5$ m.

4.1.2. Fluvial Properties

The control flood experiment instrumented by *Schmandt et al.* [2013] had discharge variations from about 240 m^3/s to 1400 m^3/s. Direct observations of water level are reported in *Kieffer* [1988] for the intermediate discharge of $Q_w = 850$ m^3/s, for which we estimate the water flow depth increased by 2 meters from 140 m^3/s to 840 m^3/s of discharge. The extrema configurations of the control flood experiment instrumented by *Schmandt et al.* [2013] do not have direct water level observations. We therefore extrapolate the flow depth measurements performed at $Q_w = 140$ m^3/s and $Q_w = 840$ m^3/s to the configurations with $Q_w = 240$ m^3/s and $Q_w = 1400$m^3/s by adding 0.5 m to both of the corresponding depth levels. A posteriori, using the water flow depth and the other channel informations cited above (see Figure 10(b) for a summary), the total discharges associated with each value of H can be approximated by using $U = 8.1\sqrt{g \sin\theta H}(H/k_s)^{1/6}$ [*Parker*, 1991] to describe the depth-average flow velocity.

4.2. Rayleigh wave Green's function Parameters

Since seismic wave parameters have not been measured on the river banks of HR. Thus, we describe surface wave velocities using the same parameters as previously for the Trisuli river, i.e. $v_{c0} = 2175$ m/s, $z_0 = 1000$ and $\xi = 0.48$ in equation 38. The value of Q_0 has been suggested by *Schmandt et al.* [2013] to plausibly be lower than 9, as $Q_0 = 9$ was found at <150 m depth in highly weathered granite [*Aster and Shearer*, 1991] and the seismic station was deployed on alluvium, i.e. on a looser material. We choose $Q_0 = 7$.

The model predictions presented hereafter are not significantly affected when varying Q_0 from 5 to 9.

The distance r_{edge} from the edge of the river to the seismic station has been reported by *Schmandt et al.* [2013] to be about 38 m at low flows, and 32 m at high flows. Since the station-to-river edge distance is similar to the river width, the source locations are weighted in the model predictions by computing force PSDs S_F over 5 m transverse sections of the river and treating the wave propagation from the location of the center of each transect to the seismic station. The value of r_0 used to describe the wave propagation from each transect is $r_0 = r_{edge} + \delta r_0$, where δr_0 is the distance of the transect center to the edge of the river. As we do not account for channel width variations, we set r_{edge} to the intermediate value of 35 m. Moreover, the length of each transect is limited by the length of the rapids section, that is set to 150 m (see Figure 9). The final, total, values of $P_{w_1}^T$ are obtained by adding up the contributions of all transects. All the parameters used to perform model predictions are listed in Table 3.

Finally, unlike in the previous Trisuli river configuration [*Burtin et al.*, 2008], a near field situation must be accounted for in the HR configuration, since $r_0 k < 1$ is reached at the low frequencies investigated (< 3 Hz). To do this, we approximate the Bessel function defined in *Aki and Richards* [2002] to describe the Green's function by $\left(1 + \left(\frac{\pi k r}{2}\right)^3\right)^{-1/6}$. This approximated form is similar to the far field approximation $\sqrt{\frac{2}{\pi k r}}$ commonly used for $r_0 k >> 1$ (see section 2.3), but exhibits a finite value of 1, as for the Bessel function, for $r_0 k << 1$.

4.3. Forward Model Predictions

Figure 11 shows the PSDs observed for $Q_w = 240$ m^3/s, $Q_w = 840$ m^3/s and $Q_w = 1400$ m^3/s during the controlled flood experiment. As in *Schmandt et al.* [2013], Figure 11(b) shows normalized PSDs, i.e. PSDs resulting from the ratio (dB difference) of PSDs recorded at the larger discharges (i.e. at $Q_w = 840$ m^3/s and $Q_w = 1400$ m^3/s) with the PSD recorded at the lowest discharge of $Q_w = 240$ m^3/s. More simply, Figure 11(a) shows the raw PSDs, i.e. the PSDs that have not been normalized in any way.

In the observed PSDs (continuous lines) of Figure 11(a), the 2 peaks centered around 0.7 Hz and 6-7 Hz shown by *Schmandt et al.* [2013] are not seen at low discharge. Also, while seismic energy at large discharge is particularly enhanced at the 2 peak frequencies described in *Schmandt et al.* [2013], the amplitude increase at larger discharges occurs over a relatively broad frequency range.

Model predictions (dashed lines) are performed using the flow depth values highlighted in Figure 10. At $Q_w = 240$ m^3/s, our model prediction does not capture the observed PSD (see Figure 11(a)). However, as river discharge increases, the uppermost part of the frequency range affected by water flow is captured by our model predictions. Both the absolute amplitude and frequency dependence of our model predictions roughly agree with the observations at $Q_w = 840$ m^3/s and $Q_w = 1400$ m^3/s in the 2 to 10 Hz frequency range. As shown in Figure 11(b), our model captures the high frequency peak reported by *Schmandt et al.* [2013] and centered around 6 to 8 Hz.

4.4. Interpretation

The agreement of our model predictions with the high frequency peak reported by *Schmandt et al.* [2013] (2 to 15 Hz), suggests that this peak is caused by turbulent flow interacting with bed roughness rather than by breaking of river surface waves, as originally interpreted by *Schmandt et al.* [2013] on the basis of acoustic energy observed in the same frequency range. We suggest that this acoustic energy may instead be caused by the coupling of the atmosphere with the ground surface waves. If this is the case, then the acoustic signal has the same origin than the seismic wave, and is also caused by force fluctuations applied on the ground. It is also possible that another river flow acoustic source is emitted at the air-water interface by a yet unidentified mechanism and by chance appears to operate in the same frequency range as that associated with the seismic noise caused by turbulent flow.

Our model fails to reproduce the PSD recorded at $Q_w = 240$ m^3/s in Figure 11(a). This disagreement is most likely due to the fact that the peaks at 1 and 17 Hz, which are not caused by turbulent flow induced noise, dominate the signal. The peak centered at 17 Hz was interpreted by *Schmandt et al.* [2013] as a site effect. If this were true, this peak should also be enhanced at increasing discharges, which is not observed. Accounting for more accurate ground seismic properties or river geometry could result in lower modelled seismic energy at frequencies larger than 10 Hz, and potentially reduce the energy at 17 Hz. However, it is also possible that the peak at 17 Hz corresponds to another source of noise, unrelated to the river. The low frequency signal reported in between 0.5 to 2 Hz by *Schmandt et al.* [2013] remains to be understood. *Schmandt et al.* [2013] interpreted this signal as resulting from fluid forces operating on the rough river bed. Instead, we suggest that this low frequency signal results from standing waves. Another possibility could be that this peak is related to the depth scale eddies forming in the production range of turbulence, which we did not include in our analysis. Eventually penetrating within the bed roughness, these depth scale eddies are expected to release larger energies than the -5/3 Kolmogorv scaling with frequency that we considered here. These hypotheses still need to be verified by future theoretical modelling and targeted measurements.

Finally, discrepancies between modelled and observed PSDs in the 2 to 10 Hz frequency range remain in Figures 11(a) and (b). First, modelled PSDs shown on Figure 11(a) exhibit a continuous decrease in power at decreasing frequency in the lower frequency part of the 2-10 Hz range, while observed PSDs seem to flatten in that range. This misfit can be due to a misrepresentation of the frequency dependence of surface-wave speeds or attenuation in our model (higher surface-wave speeds or attenuation at lower frequencies would allow a better fit). Second, in the observations, the high frequency peak centered around 6 to 8 Hz seems to shift towards lower frequencies as discharge increases. This effect could be reproduced by our model by accounting for a migration of the maximum river depth location as discharge increases. In particular, we may expect that the centrifugal force applied on the water column as the river undergoes a left turn at HR could result in larger flow depths towards the outside of the bend as discharge increases. Since the outside of the bend is located further away from the seismic station, this process could explain the migration toward lower frequencies at larger discharges.

5. Conclusion

We have developed a mechanistic model that accounts for the seismic noise caused by the interaction of turbulent flow with the river bed. Force fluctuations applied in all directions on river bed grains are explicitly accounted for from the description of the turbulent flow field, and the contribution of all river bed grains in generating seismic surface waves is evaluated to reproduce the total ground velocity power recorded at a given, nearby, seismic station.

In agreement with previous observations [*Burtin et al.*, 2008, 2011; *Schmandt et al.*, 2013], the water-flow-induced seismic noise is predicted to operate at lower frequencies than the seismic noise induced by a bedload signal. In the case of the Trisuli River in Nepal, we showed that a significant part of the seismic signal reported by *Burtin et al.* [2008] is attributable to turbulent flow. Our model in that case provides a noise base-level from which realistic bedload estimates can be inferred in the future.

We demonstrated that the distance from the river to the seismic station, ground seismic properties and hydrological characteristics such as the relative roughness of the flow and the river slope drastically change the relative amplitude as well as the frequency content of the seismic noise induced by turbulent flow versus seismic noise induced by bedload. Notably, the dependence of the respective amplitude of turbulent flow versus bedload induced noise on river-to-station distance is significant enough that both of these processes can be characterized independently at a given site by deploying seismic stations at various distances from the river (see Figure 6). In particular cases, the turbulent flow and bedload sources are distinct on a single seismic record, as it is at Hance Rapids of the Colorado River.

By prescribing relevant water flow depths and river geometries in this Hance Rapids configuration that is materialized by a distinct water flow source previously reported by *Schmandt et al.* [2013], we have shown that the absolute amplitude as well as the frequency scaling of the seismic signal can be predicted. As river bed stress is the main parameter that controls the absolute amplitude of the signal, this suggests that seismic observations can be used to invert for bed stress on the basis of this framework. Such a seismic monitoring technique, which we are currently testing in the "Les Bossons" river (Gimbert et al., Using seismic observations to quantify river mechanics: example of the "Les Bossons" river (France), *In prep.*), is particularly promising for torrential steep rivers, where significant erosion rates, bedload transport and channel migration cause direct and continuous measurements of water flow depth and river bed stress to be particularly challenging.

Besides this interesting application of monitoring flow depth or bed shear stress from seismic observations, the combination of the framework proposed in this study with specific seismic deployments may be used to better constrain the physics of the force fluctuations generated by the turbulent flow. In particular, this study relied on the assumption that the fluctuating forces operating in the various directions on a given grain present similar amplitude and spectral scalings than the fluctuating forces operating in the downstream direction. Moreover, we assumed that the force fluctuations operating in the various directions on a single grain operate independently from each other. One could tackle the validity of these assumptions by using seismic noise correlations from dense seismic networks deployed along rivers. Such a technique would allow relocating the turbulent flow sources and separating the contributions of the different turbulent forces applied in the different directions into generating seismic noise. When combined with an accurate knowledge of the ground seismic properties, such a deployment could allow inverting for the entire spectral signature of forces applied in the various directions.

As a more general comment, we find that interpreting the PSDs recorded at a given seismic station directly in terms of a source signature can be misleading, as the path effect associated with surface wave propagation strongly modifies the signal. Since seismic parameters play an important role in the model predictions, we encourage future seismological studies of rivers to investigate local ground properties from active seismic experiments, without which quantitative interpretations of seismic signals will be limited. In these cases of an appropriate knowledge of the ground seismic properties, the combination of the model proposed in this study with the bedload modelling framework proposed by *Tsai et al.* [2012] promises new and quantitative insights into the interplay between the local mechanical processes operating at the grain scale and channel morphology evolution.

Acknowledgments. We thank B. Schmandt for providing data and for interesting discussions. We thank J. G. Venditti for interesting discussions. MPL acknowledges funding from the Tectonics Observatory and the Terrestrial Hazards Observations and Reports Programs at Caltech and NSF Grant # EAR-1147381.

Notation

A	section area of a spherical river-bed grain (L^2)
$A_\perp$	section area of a grain perpendicular to the flow direction (L^2)
$A_{//}$	section area of a grain along the flow direction (L^2)
C	isotropic instantaneous fluid-grain friction coefficient (dimensionless)
$C_1 = C_L$	instantaneous liftg coefficient (dimensionless)
$C_2 = C_D$	instantaneous drag coefficient (dimensionless)
$C_3 = C_C$	instantaneous cross-stream coefficient (dimensionless)
$\bar{C}_D$	average drag coefficient (dimensionless)
$\bar{C}_L$	average lift coefficient (dimensionless)
dA	subarea of A (L^2)
D	grain diameter (L)
D_{50}	median grain size (L)
E_{u_2}	PSD of streamwise velocities in the wavenumber domain (L^2 T^{-2} Hz^{-1})
f	frequency (Hz)
f_w^{peak}	maximum frequency predicted from the water flow model (Hz)
f_b^{peak}	maximum frequency predicted from the bedload model (Hz)
f_{min}	minimum frequency of the inertial subrange (Hz)
f_{max}	maximum frequency of the inertial subrange (Hz)
f_c	corner frequency of function χ_{fl} (Hz)
F_i	instantaneous force along direction i (N)
F_i'	fluctuating force along direction i (N)
$\bar{F}_i$	average force along direction i (N)
g	acceleration due to gravity (LT^{-2})
G_{pi}	Green's function for a force applied along direction i and the component p of the seismometer
H	depth of flow (L)
H_0	reference depth of flow (L)
k	wavenumber of the Rayleigh wave (L^{-1})
k_s	roughness length (L)
k_w	wave number of turbulent eddies (L^{-1})
K	Kolmogorov constant (dimensionless)
l_c	correlation length or mixing length (L)
N_g	number of grains per unit length of river and unit grain size (L^{-2})
$P_{w_p}^g$	PSD of ground motion predicted along direction p for flow forces acting on a single grain g (L
$P_{w_p}^T$	total PSD of ground motion predicted along direction p by the water flow model (L^2 T^{-2} Hz^{-1}
$P_{b_p}^T$	total PSD of ground motion predicted along direction p by the bedload model (L^2 T^{-2} Hz^{-1})
q_b	bedload flux (L^2 T^{-1})
q_{bc}	bedload flux at transport capacity (L^2 T^{-1})
Q	quality factor at a given frequency (dimensionless)
Q_0	quality factor at $f_0 = 1$ Hz (dimensionless)
Q_w	water discharge (l T^{-}1)
r	station-to-source distance (L)
r_{edge}	station-to-river edge distance at Hance Rapids (L)
r_0	station-to-river distance (L)

r_1	Rayleigh wave eigenfunction in the vertical direction (dimensionless)
r_2	Rayleigh wave eigenfunction in the horizontal direction (dimensionless)
S_{ab}^g	cospectral density of velocities at two different locations a and b of A (N^2/Hz)
S_{u_2}	PSD of streamwise velocities in the frequency domain (L^2 T^{-2} Hz^{-1})
S_F	isotropic PSD of flow forces by unit length of river and unit grain size (N^{2}L^{-2}Hz^{-1})
S_{F_i}	PSD of flow forces acting along direction i by unit length of river and unit grain size (N^{2}L^{-2}H
$S_{F_i}^g$	PSD of flow forces acting along direction i and on a given grain g (N^{2}Hz^{-1})
t	time (T)
u_2	instantaneous streamwise velocities (LT^{-1})
u_2'	fluctuating streamwise velocities (LT^{-1})
$\bar{u}_2$	average streamwise velocities (LT^{-1})
u_*	bed shear velocity (LT^{-1})
$\dot{u}_p^g$	ground velocity induced by forces acting on grain g along direction p (LT^{-1})
U	depth averaged velocity (LT^{-1})
v_0	shear wave speed at depth z_0 (LT^{-1})
v_c	Rayleigh wave phase speed (LT^{-1})
v_{c0}	Rayleigh wave phase speed at frequency $f_0 = 1$ Hz (LT^{-1})
v_u	Rayleigh wave group speed (LT^{-1})
v_s	shear wave speed (LT^{-1})
W	river width (L)
X_1	elevation within the roughness layer (L)
z	depth below ground surface (L)
α	exponent characterizing shear velocity increase with depth (dimensionless)
δr	distance between the river section and the river edge at Hance Rapids (L)
Γ	Gamma function (dimensionless)
Γ_{12}	macroscopic mean rate of strain of the water layer (Hz)
ϵ	tubulent dissipation rate (L^2 T^{-3})
η_{Kolmo}	Kolmogorov microscale (L)
η	exponent characterizing quality factor increase with frequency (dimensionless)
θ	river slope angle (degree)
ρ_w	water density (kg L^{-3})
ρ_s	ground density (kg L^{-3})
σ_g	standard deviation of the equivalent normal distribution of the log-'raised cosine' distribution
σ_{u_i}	turbulence intensity along direction i (LT^{-1})
$\sigma_{u_i,max}$	turbulence intensity along direction i and at the roughness height (LT^{-1})
Σ_2^{ab}	cospectral density of force time-series applied at two different locations a and b over a given gr
$\mathcal{P}$	tubulent production rate (L^2 T^{-3})
φ	source-station azimuth (radian)
χ_{fl}	fluid admittance function (dimensionless)

References

Achenbach, E. (1974), Vortex shedding from spheres, *J. Fluid Mech.*, *62*(02), 209–221, doi:10.1017/S0022112074000644.

Aki, K., and P. G. Richards (2002), *Quantitative seismology*, 2nd ed., 700 pp., Univ. Sci., Sausalito, Calif.

Anderson, J. G., and S. E. Hough (1984), A model for the shape of the fourier amplitude spectrum of acceleration at high frequencies, *Bull. Seismol. Soc. Am.*, *74*(5), 1969–1993.

Aster, R. C., and P. M. Shearer (1991), High-frequency borehole seismograms recorded in the San Jacinto Fault Zone, Southern California, Part 2. Attenuation and site effects, *Bull. Seismol. Soc. Am.*, *81*(4), 1081–1100.

Bagnold, R. A. (1966), *An approach to the sediment transport problem from general physics*, 422-I, U. S. Geol. Surv., Washington, D. C.

Bayazit, M. (1976), Free surface flow in a channel of large relative roughness, *Jour. of Hyd. Res.*, *14*(2), 115–126, doi:10.1080/00221687609499676.

Belleudy, P., A. Valette, and B. Graff (2010), Passive hydrophone monitoring of bedload in river beds: First trials of signal spectral analyses, *U. S. Geol. Surv.*, (5091).

Bonnefoy-Claudet, S., C. Cornou, P.-Y. Bard, F. Cotton, P. Moczo, J. Kristek, and D. Fäh (2006), H/V ratio: a tool for site effects evaluation. results from 1-D noise simulations, *Geophys. J. Int.*, *167*(2), 827–837, doi:10.1111/j.1365-246X.2006.03154.x.

Boore, D. M., and W. B. Joyner (1997), Site amplifications for generic rock sites, *B. Seismol. Soc. Am.*, *87*(2), 327–341.

Burtin, A., L. Bollinger, J. Vergne, R. Cattin, and J. L. Nábalek (2008), Spectral analysis of seismic noise induced by rivers: A new tool to monitor spatiotemporal changes in stream hydrodynamics, *J. Geophys. Res.-Earth Surf.*, *113*(B5), B05,301, doi:10.1029/2007JB005034.

Burtin, A., R. Cattin, L. Bollinger, J. Vergne, P. Steer, A. Robert, N. Findling, and C. Tiberi (2011), Towards the hydrologic and bed load monitoring from high-frequency seismic noise in a braided river: The torrent de st pierre, french alps, *J. Hydrol.*, *408*(12), 43–53, doi:10.1016/j.jhydrol.2011.07.014.

Carollo, F., V. Ferro, and D. Termini (2005), Analyzing turbulence intensity in gravel bed channels, *J. Hydraul. Eng.*, *131*(12), 1050–1061, doi:10.1061/(ASCE)0733-9429(2005)131:12(1050).

Curle, N. (1955), The influence of solid boundaries upon aerodynamic sound, *P. Roy. Soc. Lond. A Math.*, *231*(1187), 505–514, doi:10.1098/rspa.1955.0191.

Defina, A., and A. C. Bixio (2005), Mean flow and turbulence in vegetated open channel flow, *Water Resour. Res.*, *41*(7), W07,006, doi:10.1029/2004WR003475.

Egholm, D. L., M. F. Knudsen, and M. Sandiford (2013), Lifespan of mountain ranges scaled by feedbacks between landsliding and erosion by rivers, *Nature*, *498*(7455), 475–478, doi:10.1038/nature12218.

Einstein, H., and N. L. Barbarossa (1952), River channel roughness, *Trans. Am. Soc. Civ. Eng.*, *117*, 1121–1146.

Erickson, D., and D. Mcnamara (2004), Frequency-dependent Lg Q within the continental united states, *B. Seismol. Soc. Am.*, *94*, 1630–1643, doi:10.1785/012003218.

Fernandez Luque, R., and R. Van Beek (1976), Erosion and transport of bed-load sediment, *J. Hydraul. Res.*, *14*(2), 127–144, doi:10.1080/00221687609499677.

Govi, M., F. Maraga, and F. Moia (1993), Seismic detectors for continuous bed load monitoring in a gravel stream, *Hydrolog. Sci. J.*, *38*(2), 123–132, doi: 10.1080/02626669309492650.

Howard, A. D., and G. Kerby (1983), Channel changes in badlands, *Geol. Soc. Am. Bull.*, *94*(6), 739–752, doi:10.1130/0016-7606(1983)94¡739:CCIB¿2.0.CO;2.

Hsu, L., N. J. Finnegan, and E. E. Brodsky (2011), A seismic signature of river bedload transport during storm events, *Geophys. Res. Lett.*, *38*(13), L13,407, doi: 10.1029/2011GL047759.

Kamphuis, J. W. (1974), Determination of sand roughness for fixed beds, *J. Hydraul. Res.*, *12*(2), 193–203, doi:10.1080/00221687409499737.

Kieffer, S. W. (1987), *The rapids and waves of the Colorado River, Grand Canyon, Arizona sediment and/or hydrology of the Glen Canyon Environmental Studies*, no. 87-096, D-5 in GCES report, U. S. Geol. Surv., Denver, Colorado.

Kieffer, S. W. (1988), Hydraulic map of hance rapids, grand canyon, arizona, *Tech. Rep. I - 1897-C*, U. S. Geol. Surv.

Kline, S. J., W. C. Reynolds, F. A. Schraub, and P. W. Runstadler (1967), The structure of turbulent boundary layers, *J. Fluid Mech.*, *30*(04), 741–773, doi: 10.1017/S0022112067001740.

Kolmogorov, A. (1941), The local structure of turbulence in incompressible viscous fluid for very large reynolds' numbers, *Akademiia Nauk SSSR Doklady*, *30*, 301–305.

Lamb, M. P., W. E. Dietrich, and L. S. Sklar (2008a), A model for fluvial bedrock incision by impacting suspended and bed load sediment, *J. Geophys. Res.-Earth Surf.*, *113*(F3), F03,025, doi:10.1029/2007JF000915.

Lamb, M. P., W. E. Dietrich, and J. G. Venditti (2008b), Is the critical shields stress for incipient sediment motion dependent on channel-bed slope?, *J. Geophys. Res.-Earth Surf.*, *113*(F2), F02,008, doi:10.1029/2007JF000831.

Legleiter, C. J., T. L. Phelps, and E. E. Wohl (2007), Geostatistical analysis of the effects of stage and roughness on reach-scale spatial patterns of velocity and turbulence intensity, *Geomorphology*, *83*(34), 322–345, doi:10.1016/j.geomorph.2006.02.022.

Lighthill, M. J. (1952), On Sound Generated Aerodynamically. I. General Theory, *P. Roy. Soc. Lond. A Math.*, *211*(1107), 564–587, doi:10.1098/rspa.1952.0060.

Manning, R. (1891), On the flow of water in open channels and pipes., *Transactions of the Institution of Civil Engineers of Ireland*, *20*, 161–207.

Marquis, G., and A. G. Roy (2013), From macroturbulent flow structures to large-scale flow pulsations in gravel-bed rivers, in *Coherent Flow Structures at Earth's Surface*, edited by J. G. Venditti, J. L. Best, M. Church, and R. J. Hardy, 1 edition ed., pp. 243–259, Wiley-Blackwell.

McLean, S. R., and V. I. Nikora (2006), Characteristics of turbulent unidirectional flow over rough beds: Double-averaging perspective with particular focus on sand dunes and gravel beds, *Water Resour. Res.*, *42*(10), doi:10.1029/2005WR004708.

Nakagawa, H., and I. Nezu (1981), Structure of space-time correlations of bursting phenomena in an open-channel flow, *J. Fluid Mech.*, *104*, 1–43, doi: 10.1017/S0022112081002796.

Naudascher, E., and D. Rockwell (2005), *Flow-induced vibrations: an engineering guide*, Dover Publications, Mineola, NY.

Nelson, J. M., N. W. Schmeeckle, and S. L. Shreve (2001), *Turbulence and particle entrainment*, 221–240 pp., in *Bravel-Bed River V*, edited by M. P. Morsley, New Zealand Hydrological Society, Wellington, New Zealand.

Nezu, I., and H. Nakagawa (1993), *Turbulence in open-channel flows*, Balkema, Rotterdam; Brookfield.

Nezu, I., and W. Rodi (1986), Openchannel flow measurements with a laser doppler anemometer, *J. Hydraul. Eng.*, *112*(5), 335–355, doi:10.1061/(ASCE)0733-9429(1986)112:5(335).

Nikora, V. (2011), Hydrodynamics of gravel-bed rivers: scale issues, in *Gravel Bed Rivers 6: From Process Understanding to River Restoration: 11*, edited by H. Habersack, H. Piegay, and M. Rinaldi, 1 edition ed., pp. 61–81, Elsevier Science, Amsterdam.

Nikora, V., and D. Goring (2000), Flow turbulence over fixed and weakly mobile gravel beds, *J. Hydraul. Eng.*, *126*(9), 679–690, doi:10.1061/(ASCE)0733-9429(2000)126:9(679).

Nikora, V., D. Goring, I. McEwan, and G. Griffiths (2001), Spatially averaged open-channel flow over rough bed, *J. Hydraul. Eng.*, *127*(2), 123–133, doi:10.1061/(ASCE)0733-9429(2001)127:2(123).

Nikora, V., K. Koll, I. McEwan, S. McLean, and A. Dittrich (2004), Velocity distribution in the roughness layer of rough-bed flows, *J. Hydraul. Eng.*, *130*(10), 1036–1042, doi:10.1061/(ASCE)0733-9429(2004)130:10(1036).

Norberg, C. (2003), Fluctuating lift on a circular cylinder: review and new measurements, *J. Fluid. Struct.*, *17*(1), 57–96, doi:10.1016/S0889-9746(02)00099-3.

Parker, G. (1990), Surface-based bedload transport relation for gravel rivers, *J. Hydraul. Res.*, *28*(4), 417–436, doi:10.1080/00221689009499058.

Parker, G. (1991), Selective sorting and abrasion of river gravel. II: applications, *J. Hydraul. Eng.*, *117*(2), 150–171, doi:10.1061/(ASCE)0733-9429(1991)117:2(150).

Raupach, M. R., R. A. Antonia, and S. Rajagopalan (1991), Rough-wall turbulent boundary layers, *Appl. Mech. Rev.*, *44*(1), 1–25, doi:10.1115/1.3119492.

Rickenmann, D., and A. Recking (2011), Evaluation of flow resistance in gravel-bed rivers through a large field data set, *Water Resour. Res.*, *47*(7), W07,538, doi: 10.1029/2010WR009793.

Rickenmann, D., J. M. Turowski, B. Fritschi, A. Klaiber, and A. Ludwig (2012), Bedload transport measurements at the erlenbach stream with geophones and automated basket samplers, *Earth Surf. Proc. Land.*, *37*(9), 1000–1011, doi:10.1002/esp.3225.

Roy, A. G., T. Buffin-Blanger, H. Lamarre, and A. D. Kirkbride (2004), Size, shape and dynamics of large-scale turbulent flow structures in a gravel-bed river, *J. Fluid Mech.*, *500*, 1–27, doi:10.1017/S0022112003006396.

Sarpkaya, T. (1979), Vortex-induced oscillations: A selective review, *J. Appl. Mech.*, *46*(2), 241–258, doi:10.1115/1.3424537.

Schlichting, H. (1979), *Boundary-Layer Theory*, McGraw-Hill.

Schmandt, B., R. C. Aster, D. Scherler, V. C. Tsai, and K. Karlstrom (2013), Multiple fluvial processes detected by riverside seismic and infrasound monitoring of a controlled flood in the grand canyon, *Geophys. Res. Lett.*, *40*(18), 48584863, doi:10.1002/grl.50953.

Schmeeckle, M. W., and J. M. Nelson (2003), Direct numerical simulation of bedload transport using a local, dynamic boundary condition, *Sedimentology*, *50*(2), 279–301, doi:10.1046/j.1365-3091.2003.00555.x.

Schmeeckle, M. W., J. M. Nelson, and R. L. Shreve (2007), Forces on stationary particles in near-bed turbulent flows, *J. Geophys. Res.-Earth Surf.*, *112*(F2), F02,003, doi:10.1029/2006JF000536.

Sklar, L. S., and W. E. Dietrich (2004), A mechanistic model for river incision into bedrock by saltating bed load, *Water Resour. Res.*, *40*(6), W06,301, doi: 10.1029/2003WR002496.

Taylor, G. I. (1938), The spectrum of turbulence, *Proc. Roy. Soc. Lond.*, *164*(919), 476–490, doi:10.1098/rspa.1938.0032.

Tennekes, H., and J. L. Lumley (1972), *A first course in turbulence*, The MIT, Cambridge ; London.

Tsai, V., and S. Atiganyanun (2014), Green's functions for surface waves in a generic velocity structure, *Submitted to B. Seismol. Soc. Am.*

Tsai, V. C., B. Minchew, M. P. Lamb, and J.-P. Ampuero (2012), A physical model for seismic noise generation from sediment transport in rivers, *Geophys. Res. Lett.*, *39*(2), L02,404, doi:10.1029/2011GL050255.

Tsujimoto, T. (1991), Bed-load transport in steep channels, in *Fluvial Hydraulics of Mountain Regions*, edited by P. A. Armanini and P. G. D. Silvio, no. 37 in Lecture Notes in Earth Sciences, pp. 89–102, Springer Berlin Heidelberg.

Turowski, J., and D. Rickenmann (2011), Measuring the statistics of bed-load transport using indirect sensors, *J. Hydraul. Eng.*, *137*(1), 116–121, doi:10.1061/(ASCE)HY.1943-7900.0000277.

Venditti, J. G., J. L. Best, M. Church, and R. J. Hardy (2013), *Coherent Flow Structures at Earth's Surface*, 1 edition ed., Wiley-Blackwell.

Vickery, B. J. (1966), Fluctuating lift and drag on a long cylinder of square cross-section in a smooth and in a turbulent stream, *J. Fluid Mech.*, *25*(03), 481–494, doi:10.1017/S002211206600020X.

Wang, J., Z. Dong, C. Chen, and Z. Xia (1993), The effects of bed roughness on the distribution of turbulent intensities in open-channel flow, *J. Hydraul. Res.*, *31*(1), 89–98, doi:10.1080/00221689309498862.

Whipple, K. X. (2004), Bedrock rivers and the geomorphology of active orogens, *Annu. Rev. Earth Pl. Sc.*, *32*(1), 151–185, doi:10.1146/annurev.earth.32.101802.120356.

Whipple, K. X., G. S. Hancock, and R. S. Anderson (2000), River incision into bedrock: Mechanics and relative efficacy of plucking, abrasion, and cavitation, *Geol. Soc. Am. Bull.*, *112*(3), 490–503, doi:10.1130/0016-7606(2000)112¡490:RIIBMA¿2.0.CO;2.

Wiberg, P. L., and J. D. Smith (1991), Velocity distribution and bed roughness in high-gradient streams, *Water Resour. Res.*, *27*(5), 825–838, doi:10.1029/90WR02770.

Yalin, M. S. (1992), *River mechanics*, 1st edition ed., Pergamon Press, Oxford ; New York.

Yuan, Z., and E. E. Michaelides (1992), Turbulence modulation in particulate flowsA theoretical approach, *Int. J. Multiphas. Flow*, *18*(5), 779–785, doi:10.1016/0301-9322(92)90045-I.

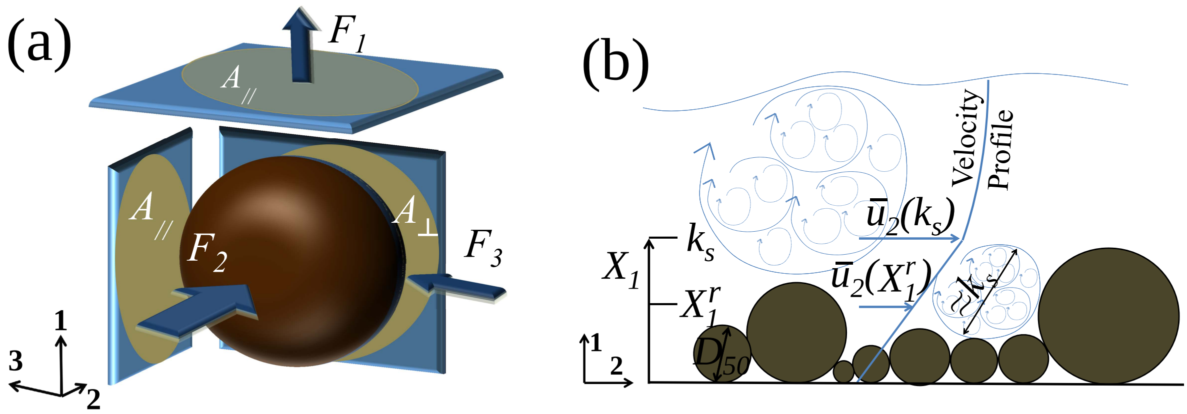

Figure 1. Schematics of the model setting. (a) Three dimensional representation of the different fluctuating components of forces acting on a given river bed grain. These forces operate over the perpendicular areas associated with the different directions. (b) Two dimensional representation of the average velocities and turbulent flow structures considered in the model. A velocity profile that deviates from the usual logarithmic profile (see equation 8) sets the average velocities within the bed roughness. The model analysis is conducted at the reference height X_1^r at which we consider turbulent eddies associated with a correlation length l_c of the order of the roughness scale k_s and travelling downstream at the average velocity $\bar{u}_2(X_1^r)$. The turbulent intensity carried by these eddies is proportional to the macroscopic shearing rate of the water layer within the bed roughness.

	Trisuli river	Hance Rapids
Seismic Parameters		
v_{c0} (m/s)	2175	2175
ξ	0.48	0.48
z_0	1000	1000
η	0	0
Q_0	20	7
r_0 (m)	600	$35 + \delta r_0$
f_0 (Hz)	1	1
River Geometry		
θ	1.4°	1°
W (m)	50	90
H (m)	4	1.64 - 4.14
D_{50} (m)	0.15	0.5
σ_g	0.52	0.7

Table 1. Default parameters used to perform model predictions at the Trisuli river and "Hance Rapids".

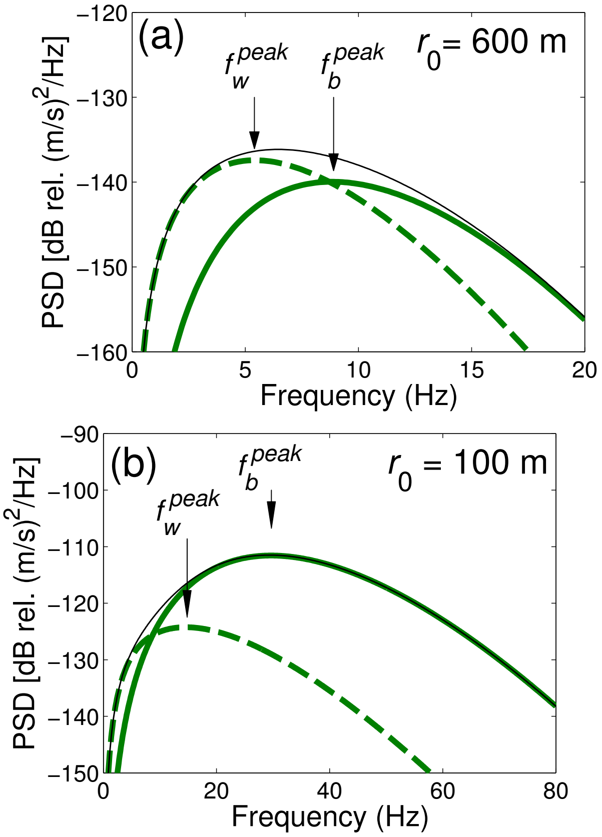

Figure 2. Modelled PSDs resulting from the turbulent flow source here presented (dashed thick green) and the bedload source presented in *Tsai et al.* [2012] (continuous thick green). Using (a) $r_0 = 600$ m and (b) $r_0 = 100$ m. Figure 2(a) and Figure 2(b) both use the default Trisuli river parameters (see main text), with $H = 4$ m and $q_b = 0.045$ m^2/s, where q_b is within the range of values inferred by *Tsai et al.* [2012]. The thin black line indicates the sum of the two model predictions. f_w^{peak} (respectively f_b^{peak}) denotes the frequency at which $P_{w_1}^T$ (respectively $P_{b_1}^T$) yields the largest value.

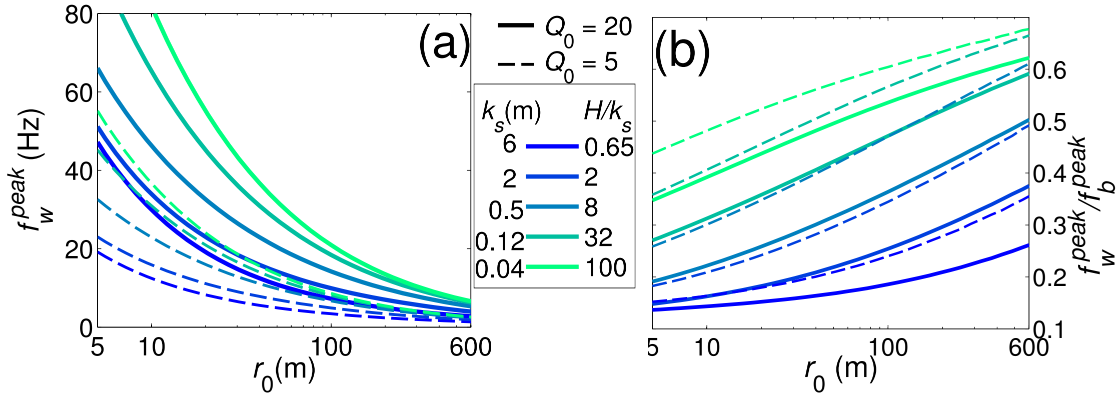

Figure 3. Turbulent flow and bedload peak frequencies f_w^{peak} and f_w^{peak}/f_b^{peak} (see Figure 2) as a function of source-station distance r_0 with varying roughness size k_s and quality factor Q_0. (a) f_w^{peak} vs. r_0. (b) f_w^{peak}/f_b^{peak} vs. r_0. Using the default Trisuli river parameters (see main text, H is kept constant and equal to 4 m) except that $D_{50} = k_s/3$ gradually varies from 0.013 m (green line) to 0.86 m (blue line). As Q_0 may exhibit significant variations from site to site, and is most likely smaller than 20 in those cases [*Schmandt et al.*, 2013], Figure 3 also includes predictions performed using $Q_0 = 5$ (thin dashed lines), in addition to the $Q_0 = 20$ considered in *Tsai et al.* [2012] (thick continuous lines).

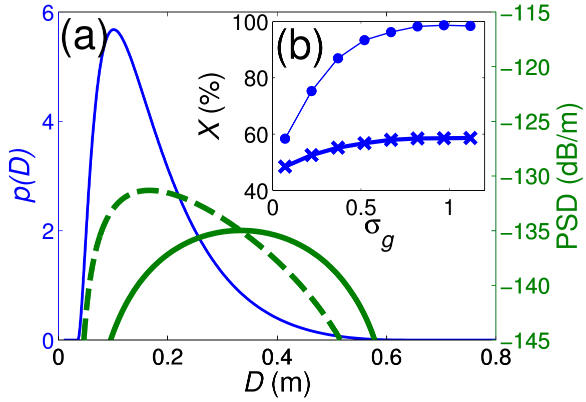

Figure 4. $P^T_{w_1}(f_w^{peak}; D)$ and $P^T_{b_1}(f_b^{peak}; D)$ resulting from the grain size distribution. (a) Log-'raised cosine' grain size probability distribution (thin blue, same as *Tsai et al.* [2012] but using $q_b = 0.045$ m^2/s) and resulting PSDs for a turbulent flow (thick dashed green) and a bedload (thick continuous green) source. (b) Grain size percentile X where D_X yields the largest PSD, as a function of σ_g for a turbulent flow (square markers) and bedload (circle markers) source. Figures 4(a) and (b) both use the default Trisuli river parameters (see main text).

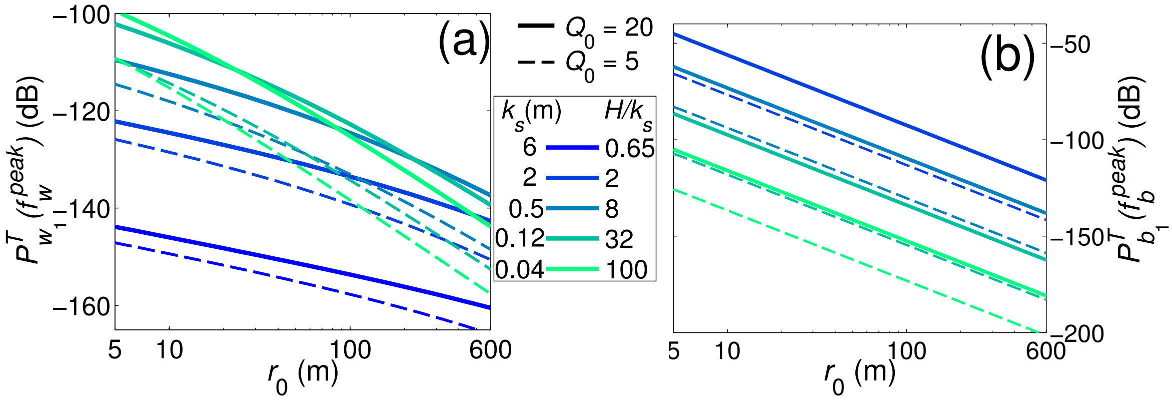

Figure 5. (a) Maximum turbulent flow induced seismic power $P^T_{w_1}(f^{peak}_w)$ and (b) maximum bedload induced seismic power $P^T_{b_1}(f^{peak}_b)$ as a function of source-station distance r_0 with varying roughness size k_s. Using the default Trisuli river parameters (see main text, H is kept constant and equal to 4 m) except that $D_{50} = k_s/3$ gradually varies from 0.013 m (light green line) to 0.86 m (dark blue line) and $q_b = q_{bc}/5$, where q_{bc} corresponds to the flux of sediments transported as bedload at transport capacity (see equation 46). The choice of $q_b = q_{bc}/5$ allows to account for the expected variations of q_b with D_{50}, while obtaining $q_b \approx 0.045$ m^2/s for the default Trisuli configuration, i.e. for $D_{50} = 0.15$ m. As Q_0 may exhibit significant variations from site to site, and is most likely smaller than 20 in those cases [*Schmandt et al.*, 2013], Figure 3 also includes predictions performed using $Q_0 = 5$ (thin dashed lines), in addition to the $Q_0 = 20$ considered in *Tsai et al.* [2012] (thick continuous lines).

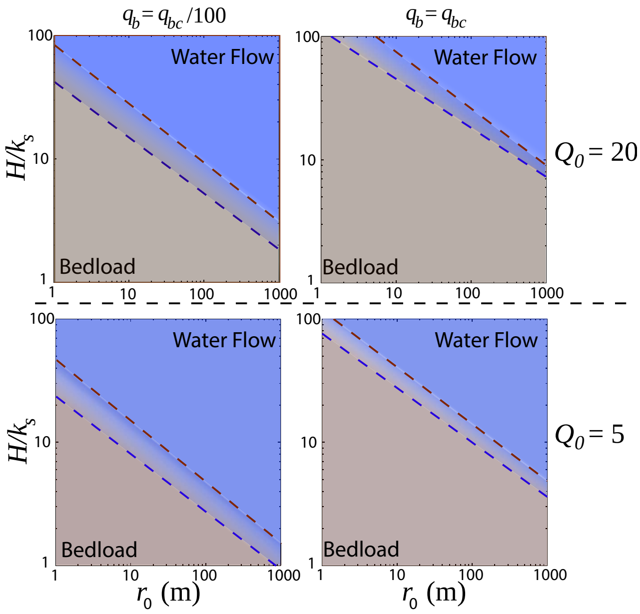

Figure 6. Phase diagrams showing the primary mechanism (i.e. either water flow or bedload) generating seismic noise at a given station as a function of its distance from the river and the apparent roughness of the flow. Blue dashed lines indicate $P^T_{w_1}(f_w^{peak}) = P^T_{b_1}(f_w^{peak})$ and brown dashed lines indicate $P^T_{w_1}(f_b^{peak}) = P^T_{b_1}(f_b^{peak})$. Using the default Trisuli river parameters (see main text, H is kept constant and equal to 4 m) except that $D_{50} = k_s/3$ has been varied from 0.013 m ($H/k_s = 100$) to 1.33 m ($H/k_s = 1$). Left diagrams calculate $P^T_{b_1}$ using $q_b = q_{bc}/100$, while right diagrams use $q_b = q_{bc}$, where q_{bc} is defined in equation 46. Top diagrams have been calculated using $Q_0 = 20$, while $Q_0 = 5$ has been used for bottom diagrams. The blue region corresponds to $P^T_{w_1}(f_w^{peak}) > P^T_{b_1}(f_w^{peak})$ (i.e. turbulent flow induced noise dominates in its frequency range), while the brown region corresponds to $P^T_{b_1}(f_b^{peak}) > P^T_{w_1}(f_b^{peak})$ (i.e. bedload induced noise dominates in its frequency range). There exists a narrow range (between dashed lines) for which both turbulent flow and bedload induced noise dominate in their respective frequency range.

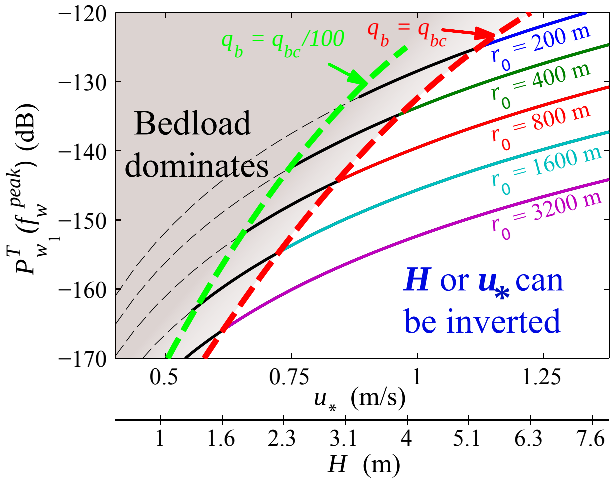

Figure 7. Maximum seismic power $P^T_{w_1}(f_w^{peak})$ induced by turbulent flow as a function of shear velocity u_* or flow depth H for various distances r_0 from the river. Using the default Trisuli river parameters (see main text) except that H is varied from 0.5 m to 8 m, and various values of r_0 ranging from 200 m (blue line) to 3200 m (purple line) are selected. The dashed lines indicate the location where the amplitude of bedload induced noise is similar to the amplitude of turbulent flow induced noise, i.e. $P^T_{w_1}(f_w^{peak}) = P^T_{b_1}(f_w^{peak})$. The red dashed line uses $q_b = q_{bc}$ to calculate $P^T_{b_1}(f_w^{peak})$, while the green dashed line uses $q_b = q_{bc}/100$. The domain lying to the right of the respective dashed lines (unfilled) corresponds to the domain where shear velocity at bed (or water flow depth) can be inverted from seismic data.

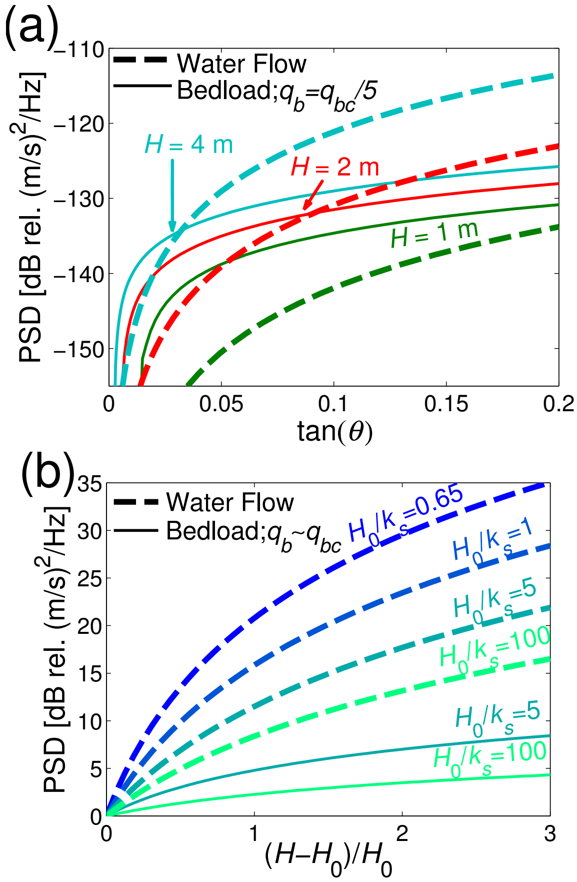

Figure 8. (a) $P_w^T(f_w^{peak})$ vs. $S = \tan(\theta)$ and (b) $\Delta P_w^T(f_w^{peak})$ (dashed lines) and $\Delta P_w^T(f_w^{peak})$ (continuous lines) vs. normalized depth variation $(H - H_0)/H_0$, where H_0 stands for a reference, initial, water flow depth. Here, Δ indicates that a PSD variation is evaluated, i.e. all data points of Figure 8(b) have been normalized by the PSD calculated at H_0. Figures 8(a) and 8(b) both use the default Trisuli river parameters except that both H and θ are varied in (a), while k_s, θ, H and H_0 are varied in (b). As modelled PSDs in (b) are normalized by PSDs obtained at H_0 and k_s, the results do not depend on the absolute values of H_0 and k_s, and also do not depend on the constant used to scale q_b with q_{bc}.

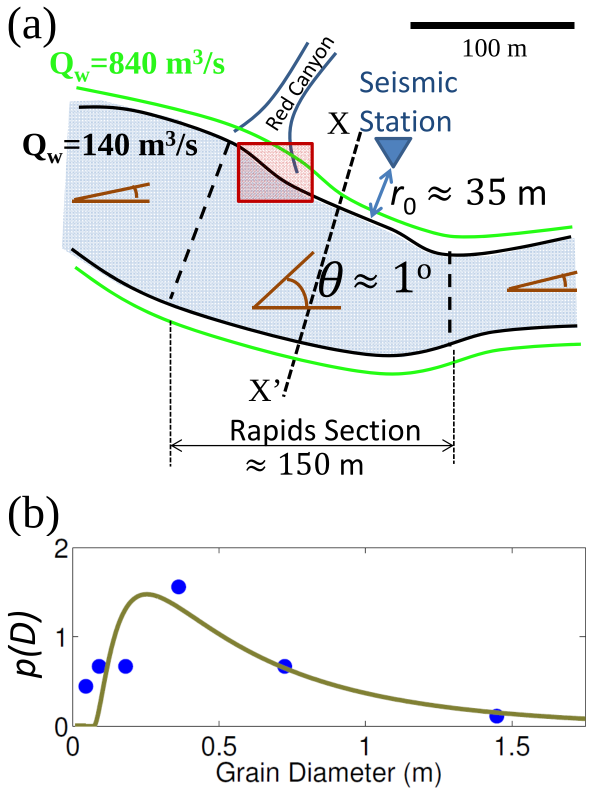

Figure 9. Channel geometry and river bed grain sizes associated with the Hance Rapids section of Grand Canyon. (a) Schematics of the river channel at $Q_w = 140$ m^3/s (black curve) and $Q_w = 840$ m^3/s (green curve) (modified from *Kieffer* [1988]). The red, smaller, rectangle indicates the location where the grain size distribution shown in (b) was measured. The transect materialized by the black line between X and X' corresponds to the location of the cross section shown on Figure 10(a). (b) Measured (blue dots) and modelled (brown line) grain size distribution. The measurements have been reported from *Kieffer* [1987] and the modelled distribution is calculated using $D_{50} = 0.5$ m and $\sigma_g = 0.7$ in the log-'raised cosine' distribution.

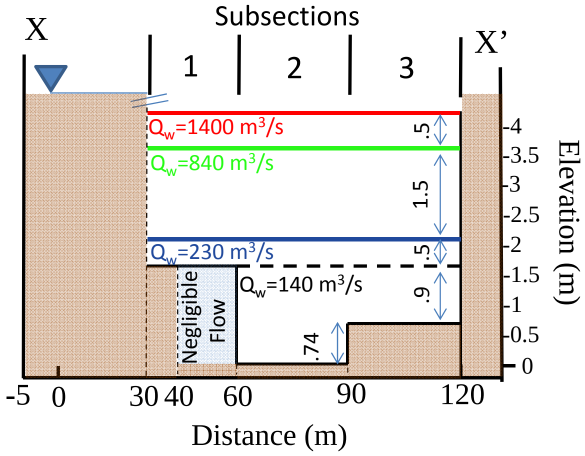

Figure 10. River bed topography and water flow depth values considered in model predictions (approximated from the measurements of the X-X' cross section reported in *Kieffer* [1988]). The water flow depths associated with $Q_w = 140$ m^3/s and $Q_w = 840$ m$^3/s$ are constrained by direct observations [*Kieffer*, 1988], while H values of $Q_w = 240$ m^3/s and $Q_w = 1400$ m$^3/s$ have been extrapolated by assuming a typical average velocity profile.

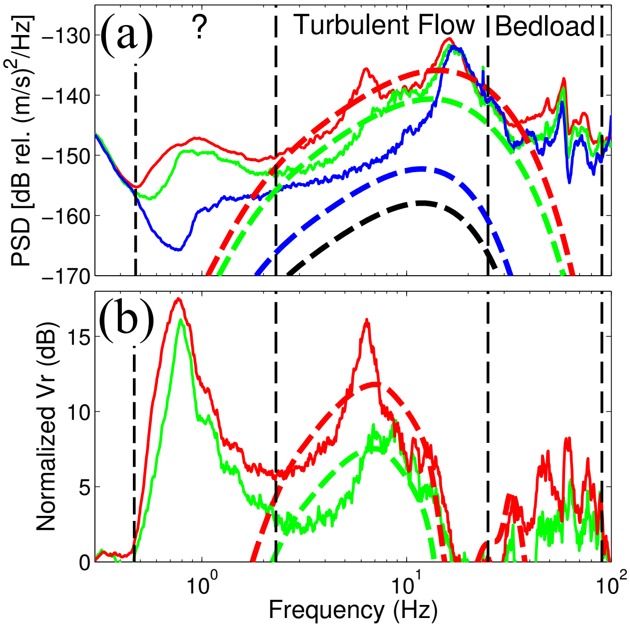

Figure 11. Model predictions of PSDs recorded at Hance Rapids of the Colorado river. (a) Observed (continuous lines) and modelled (dashed lines) PSDs at the various discharges $Q_w = 140$ m^3/s (black line, $H = 0.64$ m), $Q_w = 230$ m^3/s (blue lines, $H = 2.14$ m), $Q_w = 840$ m^3/s (green lines, $H = 3.64$ m), $Q_w = 1400$ m^3/s (red lines, $H = 4.14$ m). (b) Normalized observed (continuous lines) and modelled (dashed lines) PSDs selected at $Q_w = 840$ m^3/s and $Q_w = 1400$ m^3/s. These PSDs have been divided (dB difference) by the reference PSD observed at $Q_w = 230$ m^3/s. Water levels associated with discharges are shown on Figure 10. No seismic measurements are available for the black dashed line associated with the reference configuration $Q_w = 140$ m^3/s documented in *Kieffer* [1988].